MODAL ANALYSIS OF BLOOD FLOW IN BRAIN ANEURYSMS

A Paper
Submitted to the Graduate Faculty
of the
North Dakota State University
of Agriculture and Applied Science

By

Davina Jane Kasperski

In Partial Fulfillment of the Requirements
for the Degree of
MASTER OF SCIENCE

Major Department:
Biomedical Engineering

November 2022

Fargo, North Dakota

NORTH DAKOTA STATE UNIVERSITY

Graduate School

Title

MODAL ANALYSIS OF BLOOD FLOW IN BRAIN ANEURYSMS

By

Davina Jane Kasperski

The supervisory committee certifies that this paper complies with North Dakota State University's regulations and meets the accepted standards for the degree of

MASTER OF SCIENCE

SUPERVISORY COMMITTEE:

Dr. Trung Bao Le

Chair

Dr. Dharmakeerthi Nawarathna

Dr. Christopher Whitsel

Approved:

November 17, 2022

Date

Dr. Annie Tangpong

Department Chair

ABSTRACT

The evolution of blood flow is vital in understanding the pathogenesis of brain aneurysms. Several past studies have shown evidence for a turbulent inflow jet at the aneurysm neck. Although there is a great need for analyzing inflow jet dynamics in clinical practice, data summarized in non-invasive modalities such as Magnetic Resonance Imaging or Computed Tomography are usually limited by spatial and temporal resolutions, and thus cannot account for the hemodynamics. In this paper, Dynamic Mode Decomposition (DMD) is used to pinpoint the dominant modes of the inflow jet in patient-specific models of sidewall aneurysms. This paper aims to prove that the dynamic modes are inflow jet interaction with the distal wall in addition to the hemodynamics of the parent artery. Our work indicates that DMD is an essential tool for analyzing blood flow patterns of brain aneurysms and is a promising tool to be used in *in vivo* context.

ACKNOWLEDGEMENTS

This paper would not be possible without the assistance from Sanford Health and the financial support from the Biomedical Engineering Program (BME Graduate Fellowship) and the ND EPSCoR Office at NDSU (ND-ACES Project -NSF# 1946202). Special thanks goes to my paper advisor, Dr. Trung Le, and other members of our laboratory at NDSU (Lahcen Akerkouch and Berkay Koyuncu) for their technological guidance, patience, and encouragement. Finally, I want to thank my family and friends for their encouragement, support, and patience.

DEDICATION

This paper is dedicated to my friend Samantha Muth. Sam, inspired me to pursue a masters in Biomedical Engineering, and I wouldn't have gotten this far if not for her.

TABLE OF CONTENTS

ABSTRACT iii

ACKNOWLEDGEMENTS iv

DEDICATION v

LIST OF TABLES viii

LIST OF FIGURES ix

1. INTRODUCTION 1

1.1. The clinical aspect of brain aneurysms 1

1.2. The anatomy of brain aneurysms 1

1.3. Measuring the rupture risk 3

1.4. The role of Computational Fluid Dynamics in disease monitoring 3

1.4.1. Modeling blood flow dynamics 4

1.4.2. Hemodynamics of brain aneurysms in patient-specific anatomies 5

1.5. Predicting rupture risk using modal analysis of flows 6

1.6. Modal analysis of blood flows 6

1.6.1. Eigenvalue Decomposition vs Singular Value Decomposition 7

1.6.2. Proper Orthogonal Decomposition 7

1.6.3. Dynamic Mode Decomposition (DMD) 8

1.7. Summary 9

2. METHODOLOGY 11

2.1. Anatomical models 11

2.2. Extracting a 3D Model From Patient Data 11

2.3. Computational Setup 13

2.4. Numerical simulations of blood flow dynamics 15

2.5. DMD analysis procedure 16

2.6. The MATLAB code for DMD analysis 18
3. RESULTS 27
3.1. Model validation: Simulation of a model for axisymmetric stenosed vessel 27
3.2. Blood flow structures in the aneurysm models 29
3.2.1. Two-dimensional flow patterns on representative planes 29
3.2.2. Three-dimensional flow structures 36
3.3. DMD analysis 44
3.3.1. DMD Spectra 52
4. CONCLUSIONS 53
REFERENCES 55

LIST OF TABLES

Table Page

2.1. Measured dimensions for eleven selected aneurysm models from the Aneurisk project (`https://github.com/permfl/AneuriskData`). These dimensions were calculated in Paraview and verified using the dimensions from the Aneurisk data. 11

2.2. The computational cases for all models. The size of the structural grid is indicated in the i, j, k directions. 16

3.1. Modal frequencies generated from Matlab code. Primary mode, secondary mode, and tertiary mode correspond to modes 1, 2, and 3 respectively. 52

LIST OF FIGURES

Figure Page

1.1. Labeled model of a Circle of Willis arterial network. (Source: wikipedia.org). 2

2.1. Illustration of a y-plane view of a sample fluid mesh. This illustration shows the fluid mesh setup for each aneurysm as previously mentioned where D represents the diameter of the parent artery and the blue outline is the bounds of the fluid mesh. 13

2.2. Extracted aneurysms listed as follows: top row (from left to right), C0002, C0006, and C0014; second row (from left to right), C0016, C0034, and C0036; third row (from left to right), C0042, C0067, and C0075; bottom row (from left to right), C0085 and C0088b. 14

2.3. Visualization of the DMD setup in Paraview. Here is shown the extracted subset of C0002's aneurysm. 18

3.1. Mesh of Stenosed vessel. 27

3.2. Animation Still shot of CFD model of blood flow in an Axisymmetric Stenosed Vessel . 28

3.3. Animation Still shot of CFD model of blood flow showing flow velocity streamlines in an Axisymmetric Stenosed Vessel. 28

3.4. C0002 Flow Velocity xz-plane slice at timesteps (from left to right) 8200, 8600, 9000, 9400, 9800, 10200, 10600, 11000, 11400, and 11800; where 9000 is the time of peak velocity. 29

3.5. C0006 Flow Velocity z-plane slice at timesteps (from left to right) 8200, 8600, 9000, 9400, 9800, 10200, 10600, 11000, 11400, and 11800; where 9000 is the time of peak velocity. . . 30

3.6. C0014 Flow Velocity z-plane slice at timesteps (from left to right) 8200, 8600, 9000, 9400, 9800, 10200, 10600, 11000, 11400, and 11800; where 9000 is the time of peak velocity. . . 31

3.7. C0016 Flow Velocity x-plane slice at timesteps (from left to right) 8200, 8600, 9000, 9400, 9800, 10200, 10600, 11000, 11400, and 11800; where 9000 is the time of peak velocity. . . 31

3.8. C0034 Flow Velocity z-plane slice at timesteps (from left to right) 8200, 8600, 9000, 9400, 9800, 10200, 10600, 11000, 11400, and 11800; where 9000 is the time of peak velocity. . . 32

3.9. C0036 Flow Velocity z-plane slice at timesteps (from left to right) 8200, 8600, 9000, 9400, 9800, 10200, 10600, 11000, 11400, and 11800; where 9000 is the time of peak velocity. . . 33

3.10. C0042 Flow Velocity xz-plane slice at timesteps (from left to right) 8200, 8600, 9000, 9400, 9800, 10200, 10600, 11000, 11400, and 11800; where 9000 is the time of peak velocity. 33

3.11. C0067 Flow Velocity z-plane slice at timesteps (from left to right) 8200, 8600, 9000, 9400, 9800, 10200, 10600, 11000, 11400, and 11800; where 9000 is the time of peak velocity. . . 34

3.12. C0075 Flow Velocity xz-plane slice at timesteps (from left to right) 8399, 8799, 9199, 9599, 9999, 10399, 10799, 11199, 11599, and 11999; where 9199 is the time of peak velocity. 34

3.13. C0085 Flow Velocity z-plane slice at timesteps (from left to right) 8200, 8600, 9000, 9400, 9800, 10200, 10600, 11000, 11400, and 11800; where 9000 is the time of peak velocity. . . 35

3.14. C0088b Flow Velocity xyz-plane slice at timesteps (from left to right) 8200, 8600, 9000, 9400, 9800, 10200, 10600, 11000, 11400, and 11800; where 9000 is the time of peak velocity. 36

3.15. Flow pattern inside C0002's aneurysm. The velocity field at the peak systole is visualized by the streamlines. 37

3.16. Flow pattern inside C0006's aneurysm. The velocity field at the peak systole is visualized by the streamlines. 37

3.17. Flow pattern inside C0014's aneurysm. The velocity field at the peak systole is visualized by the streamlines. 38

3.18. Flow pattern inside C0016's aneurysm. The velocity field at the peak systole is visualized by the streamlines. 39

3.19. Flow pattern inside C0034's aneurysm. The velocity field at the peak systole is visualized by the streamlines. 40

3.20. Flow pattern inside C0036's aneurysm. The velocity field at the peak systole is visualized by the streamlines. 40

3.21. Flow pattern inside C0042's aneurysm. The velocity field at the peak systole is visualized by the streamlines. 41

3.22. Flow pattern inside C0067's aneurysm. The velocity field at the peak systole is visualized by the streamlines. 42

3.23. Flow pattern inside C0075's aneurysm. The velocity field at the peak systole is visualized by the streamlines. 42

3.24. Flow pattern inside C0085's aneurysm. The velocity field at the peak systole is visualized by the streamlines. 43

3.25. Flow pattern inside C0088's sidewall aneurysm, C0088b. The velocity field at the peak systole is visualized by the streamlines. 44

3.26. C0002 DMD modes 1 (red), 2 (green), and 3 (blue). Modes 2 and 3 almost completely overlap for this case, hence why only specs of blue can be seen. 45

3.27. C0006 DMD modes 1 (red), 2 (green), and 3 (blue). 45

3.28. C0014 DMD modes 1 (red), 2 (green), and 3 (blue). 46

3.29. C0016 DMD modes 1 (red), 2 (green), and 3 (blue). 46

3.30. C0034 DMD modes 1 (red), 2 (green), and 3 (blue). 47

3.31. C0036 DMD modes 1 (red), 2 (green), and 3 (blue). 47

3.32. C0042 DMD modes 1 (red), 2 (green), and 3 (blue). 48
3.33. C0067 DMD modes 1 (red), 2 (green), and 3 (blue). 48
3.34. C0075 DMD modes 1 (red), 2 (green), and 3 (blue). 49
3.35. C0085 DMD modes 1 (red), 2 (green), and 3 (blue). 49
3.36. C0088b DMD modes 1 (red), 2 (green), and 3 (blue). 50

1. INTRODUCTION

1.1. The clinical aspect of brain aneurysms

Intracranial Aneurysm is a common cerebrovascular disorder that causes swelling in the blood vessels of the brain [32]. It is estimated that this disorder affects 2% to 5% of all adults worldwide [32]. In the United States alone, 1 out of every 50 people have or will have an unruptured aneurysm [33]. Typically aneurysms are more common in persons between 35 and 60 years with women more likely than men to develop one if they are over the age of 40 [33]. Furthermore, patients can develop multiple aneurysms. Approximately 10-30% of patients currently have or will have multiple aneurysms [36].

Nearly all aneurysms are discovered purely by accident, causing problems such as pressing up against cranial nerves or hemorrhaging [13, 23, 24]. Aneurysms, themselves, vary in shape, size, and complexity. Additionally, aneurysms can develop two or more branches becoming what is called a bifurcation aneurysm [24] and thus, have increased complexity. Moreover, aneurysms can cause serious problems such as pressing up against cranial nerves as was previously mentioned, leaking blood into the brain, or rupture which can cause hemorrhaging [13, 23].

Hence, if an aneurysm ruptures, it can pose life-threatening consequences. Thus, rupture risk analysis of existing aneurysm(s) in a patient is crucial. Luckily, less than 1% of aneurysms rupture [33]. Despite this low risk, roughly half a million globally die each year to a ruptured aneurysm [25]. As a result, treatment of the aneurysm is required to prevent further issues. Additionally, the more complex an aneurysm is, the harder it is to calculate rupture risk.

1.2. The anatomy of brain aneurysms

Roughly 85% of all aneurysms occur in the circle of Willis [28]. The circle of Willis (CoW) is a major artery network located at the base of the brain. The CoW consists of an arterial ring and other artery vessels that branch off from the ring as shown in Figure 1.1. The ring, itself is formed by the posterior communicating arteries (PComA) and the anterior communicating arteries (AComA) which act as a highway between the brain's posterior and anterior [20]. The anterior cerebral arteries (ACA) feed into the AComA. The vertebral arteries (VA) join at the basilar artery (BA) which feeds into the posterior side of the ring. Beneath the BA on either side the posterior

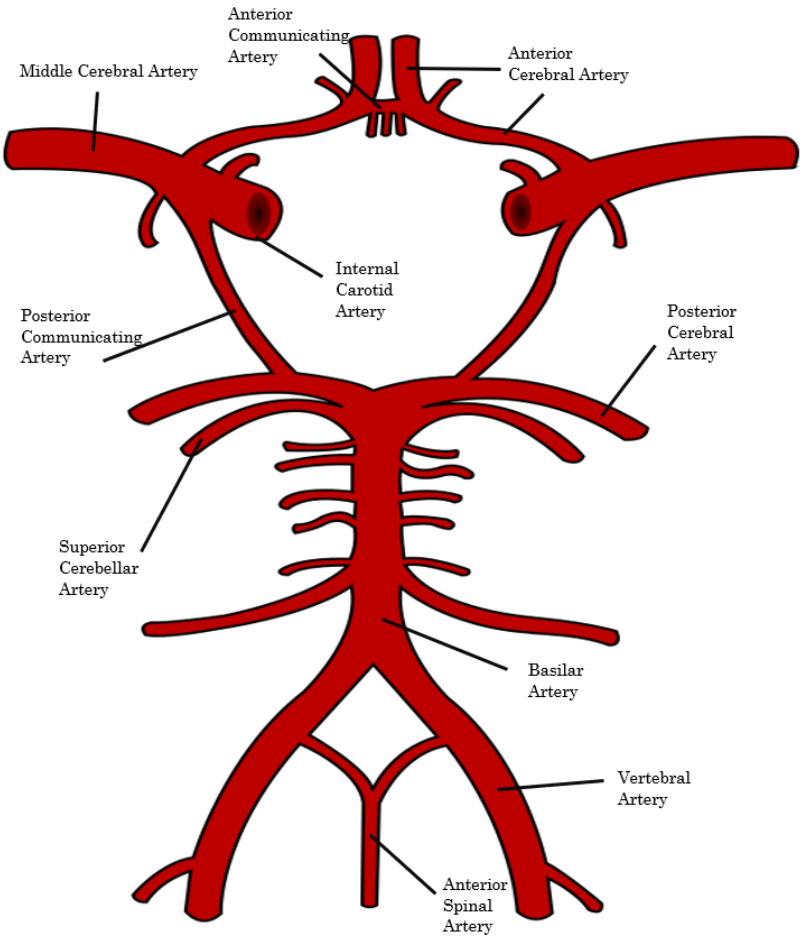

Figure 1.1. Labeled model of a Circle of Willis arterial network. (Source: wikipedia.org).

cerebral arteries (PCA) branch off of the ring. On the left and right sides of the ring branch out the middle cerebral arteries (MCA) close to the brain's anterior outside the ring along with the internal carotid arteries (ICA) close to the brain's anterior inside the ring.

However, only about 49% of the population have a complete CoW network [20]. Liang et al describe in their paper that are a total of nine possible CoW configurations including a complete CoW [20]. The other configurations have missing or incomplete artery pairs of the list of artery pairs previously discussed.

A single aneurysm can take on one of two different shapes either saccular or fusiform. A saccular aneurysm is a bulge that is attached on one side of the artery [24]. In contrast, fusiform aneurysms are a bulge that surrounds the edges of the artery [24]. Saccular aneurysms are generally more common [10], and thus will serve as the primary focus of our research.

1.3. Measuring the rupture risk

Current risk factor calculators take into account the patient's history, as well as the location, orientation, size, and complexity of the aneurysm [12, 13]. Due to the complexity of some aneurysms, finding the right treatment can be a challenge. Treatment options available for brain aneurysms include surgical clipping, endovascular coiling, and more recently flow diverters [22].

In a surgical clipping procedure, the neurosurgeon inserts a metal clip at the base of the aneurysms to stop the flow to it [22]. Unlike surgical clipping, endovascular coiling is less invasive, in that the neurosurgeon inserts a catheter into an artery typically in your groin, and guides it through your body to the aneurysm [22]. Like many surgical treatments, they are not free of risks. Bleeding in the brain or loss of flow to the brain can occur, and even though coiling is less invasive, the aneurysm can reopen later on [22] However, some complex brain aneurysms are not fixable by the first two treatments and are then typically repaired using flow diverter devices [24]. Flow into the lesion is reduced in this way while preserving the flow to the side branches and distal vasculature [24]. The tight mesh of flow diverters (FD) allows for resistance to flow across the device's surface [24]. Due to the various options, treatment decisions are often based on a neurosurgeon's preference and intuition as the treatment process is often challenging due to the microsurgeries that are required [24].

This is where medical imaging comes into play. Several researchers in the field of computational fluid dynamics aim to solve this problem. The structures of aneurysms via computed tomography (CT) or magnetic resonance imaging (MRI), can render detailed fluid flow simulations to a reasonable scale as been shown by several studies [5, 24, 35, 36]. This large assortment of data allows for the velocity and pressure fields to be expressed in great detail. However, there is a significant gap between numerical analysis and clinical practice [4, 39] as determining the right treatment for a specific patient from raw data is not an easy task. In this study, we aim to present the findings in a detailed methodical report describing the features of the flow. The report in turn can serve as a way to help neurosurgeons decide on the best treatment for a specific patient.

1.4. The role of Computational Fluid Dynamics in disease monitoring

It was previously stated that current risk factor calculators take into account the patient's history as well as the configuration of the aneurysm in space [12, 13]. This approach is not very

specific as this is what would be called a black box approach, i.e. we are looking at the aneurysm from the outside. Moreover, current risk factor calculators lack necessary data related to intra-aneurysmal blood flow dynamics [24]. As a result, many current risk factor calculators cannot predict unstable aneurysms accurately [24]. Blood fluid dynamics more commonly referred to as hemodynamics can help with the measure of rupture risk [38].

Hemodynamics of blood in brain aneurysms is analyzed using image-based computational fluid dynamics. Computational fluid dynamics (CFD), the analysis of fluid flows using numerical computations [37], is useful in determining and visualizing the underlying hemodynamics. Furthermore, previous studies have shown that wall shear stress is associated with the growth and rupture of an intracranial aneurysm [29, 38]. Ultimately, the holy grail of hemodynamics is directly measuring wall shear stress (WSS) within the aneurysm, the force exerted on the aneurysm wall [24]. Fortunately for us, hemodynamics can indirectly measure WSS using image-based CFD [38].

It is also worth noting, aneurysms will only vibrate if the instabilities have sufficient energy close to that of its wall [13]. In other words, an aneurysm ruptures when the stress within the wall exceeds the strength of the wall [21]. This vibration may play into the possible maladaptive response of the cells within the wall that in turn leads to the growth of the aneurysm and its eventual rupture [13]. Hence, why WSS affects the life cycle of an aneurysm [29].

Most computational fluid dynamics models cannot account for flow instabilities, but high-fidelity (high precision) CFD can [13]. This coincides with the fact that spatial resolution determines the accuracy of WSS estimations [38]. One such aneurysm case that has a higher chance of flow instabilities is bifurcation aneurysms in that they are more complex [13]. High-frequency flow instabilities, sometimes with non-negligible power into the hundreds of Hz, can arise from jet instabilities as the flow enters the aneurysm which consequently is consistent with direct numerical simulations of transient turbulence in a stenosed carotid bifurcation model [13]. Thus, this is more than just a coincidence.

1.4.1. Modeling blood flow dynamics

Blood, in the CFD model, is assumed to be an incompressible Newtonian fluid in that it has a constant viscosity and density as blood is mostly water [1]. However, sometimes the blood vessel size is too small for this assumption and it is approximated as a Navier-Stokes fluid or as a non-Newtonian fluid [1]. Typically, blood has a higher viscosity than plasma, but as hematocrit

levels rise so does viscosity causing blood to act more like a non-Newtonian fluid, especially at fairly low shear rates [1].

In several CFD studies of laminar-turbulent transitional flow in the human brain, various methodologies were used namely, Reynolds-averaged Navier-Stokes (RANS), large eddy simulation (LES), and direct numerical simulation (DNS) [31]. In RANS modeling, two equations are used to produce a turbulence model, the equation for the medium and the transitional flow model [31].

1.4.2. Hemodynamics of brain aneurysms in patient-specific anatomies

The study of blood flow dynamics in normal cerebral arteries and the CoW are crucial to understanding the hemodynamics of aneurysms and how they develop [29]. Blood flow into an aneurysm can vary greatly depending on the aneurysm's size, shape, orientation, and location [8, 24, 29]. Generally, blood will fill the aneurysm before continuing its normal course. In the case of saccular aneurysms, blood flow acts vaguely similar to water entering a circular wave pool. Blood flows, filling the aneurysm before leaving and continuing down the vessel [8]. The larger the aneurysm the longer blood flow is halted by the aneurysm so to speak. This in turn slows the flow of blood to the rest of the brain.

Intra-aneurysmal flow patterns are usually simple and stable or complex and turbulent [29]. Simple flow patterns might consist of a single vortex region or a vortical structure in an aneurysm [29]. The main vortex may stay fixed or move during the cardiac cycle [29]. More complex flow patterns typically have more than one recirculation region which may remain stable, move, or behave independently of each other [29]. Blood flow dynamics in aneurysms depends not only on the size, shape, orientation, and location of the aneurysm but on the size and shape of the parent artery as well [29, 39].

In some cases, blood flows straight into the aneurysm colliding against the aneurysm wall creating a region of high wall shear stress (WSS) [29]. Other aneurysms have an inflow jet that generates slower flow resulting in a more uniform WSS [29]. WSS, in essence, is a diverging mechanical stress which acts on the vessel lumen [39]. WSS vectors, themselves tend to vary relative to the aneurysm size, characterization of the inflow jet, and the location of the inflow jet; this in turn creates different regions of elevated WSS [29, 39]. However, the issue is three-dimensional WSS needs there to be a complete velocity gradient tensor which over a decade ago was an impossible task [38].

Xiaolin Wu and their colleagues presented the similarities and differences in the velocity field, vortex, and WSS distributions obtained by 4D Flow MRI, Stereoscopic Particle Image Velocimetry (Stereo-PIV), Tomographic Particle Image Velocimetry (Tomo-PIV), and computational fluid dynamics (CFD). [38]. Wu and their colleagues reconstructed and 3-D printed a patient-specific aneurysm from 4D Flow 7-Tesla MRI, and then tested the different imaging techniques. [38]. Their results showed all modalities were able to describe the flow characteristic of a high-velocity inflow jet as well as its vortex ring structure. [38]. Although the qualitative agreement in WSS was found across all modalities, there was wide variability in absolute WSS scores [38]. In their study, Tomo-PIV resulted in a higher WSS and better velocity agreement with CFD than Stereo-PIV did. [38]. This confirms spatial resolution is the main factor in the underestimation of WSS. [38].

1.5. Predicting rupture risk using modal analysis of flows

MacDonald and their colleagues stated that spectrograms of cardiovascular CFD data can illustrate spectro-temporal hemodynamic trends. [21]. With this in mind, they set out to test whether the presence of horizontal harmonic bands in spectrograms can be linked to aneurysm rupture status. [21]. They found that the visual nature of spectrograms allows for a better ability to compare the power, duration, and quality of flow instabilities between the aneurysm cases. [21]. To test their hypothesis they conducted univariate logistic regression on each of the hemodynamic metrics and computed significant tests. [21]. However, MacDonald and their colleagues did find statistically significant evidence with only one of the hemodynamic metrics. [21]. Furthermore, they found that harmonic concentration of spectral power in sac spectrograms had a stronger association with rupture status than hemodynamic predictors. [21].

Any number of flows can share several of the same parameters and/or features such as the Reynolds number [3, 27, 30]. Other features include flow instabilities, vortex pairing, merging, etc., [30]. Many of these features can be identified using visualizations of the flow, even under turbulent conditions [2, 30]. One would expect to be able to extract features using modal analysis [2, 30] as explained below.

1.6. Modal analysis of blood flows

Even at the basic level, some fluids can express complex flow patterns that vary with time and space [30]. As a result, extracting the most important features, or modes, is often the first step in the analysis of such flows [30]. This is where modal decomposition comes into play. The

decomposition of the important modes can be done using one of several methods. For our research, we used the following modal decomposition method, Dynamic Modal Decomposition (DMD). Before one can understand DMD, one needs to understand where it comes from.

1.6.1. Eigenvalue Decomposition vs Singular Value Decomposition

Eigenvalue decomposition is conducted on square matrices, whereas singular value decomposition can be applied to rectangular matrices [30]. Analyses that use eigenvalue decomposition are typically utilized when the operator of the domain and range matrices are the same [30, 34]. For any matrix $A \in \mathbb{C}^{n\times n}$, there exists an eigenvector, $v \in \mathbb{C}^n$ and an eigenvalue, $\lambda \in \mathbb{C}$ such that $Av = \lambda v$ [30]. For this statement to be true every eigenvector has only one unique eigenvalue [30].

Eigenvalue decomposition expands the formula, $Av = \lambda v$, by applying the multiplication in an iterative manner [30]. This results in the equation $AV = \Lambda V$ where $V = [v_1, v_2, ...v_n] \in \mathbb{C}^{n\times n}$ and $\Lambda = [\lambda_1, \lambda_2, ...\lambda_n] \in \mathbb{C}^{n\times n}$ [30]. For eigenvalue decomposition to work, matrix A must have a complete set of n linearly independent eigenvectors [30].

For any eigenvalue, λ_j, the real and imaginary parts describe the growth rate while each eigenvector, v_j, explains how often and in the direction the state variable changes. Also, for a linear system to be stable the real part of each eigenvalue must be less than zero or in other words, must fall on the left-hand side of the complex plane [30].

Singular value decomposition (SVD) expands the idea of eigenvalue decomposition, in that SVD can be applied to a rectangular matrix instead of a square matrix [30]. SVD allows for dimension reduction which can be used for low-rank matrix approximations as well as rotation around a vector [9, 30]. Like eigenvalue decomposition, SVD can be used as a means of demonstrating the effect of matrix operations by multiplying scalars in the appropriate directions [30]. In the two following modal decomposition methods, SVD is used [30].

1.6.2. Proper Orthogonal Decomposition

Proper orthogonal decomposition (POD) is a type of modal decomposition that derives modes from optimizing the squared mean of the field variable [30]. POD stands as one of the most popular techniques in evaluating fluid flow [30]. The POD algorithm takes individual scalars or data points from a vector field, $q(\xi, t)$, concerning discrete points in space-time as inputs [30]. An individual scalar or point in a vector field in this way is what is called a snapshot. On the other

hand, the outputs are sets of orthogonal modes $\phi_j(\xi)$, their corresponding temporal coefficients $a_j(t)$, and energy levels λ_j, ordered by the relative amount of energy [30].

For the given flow-field $q(\xi, t)$, snapshots of the flow-field are represented as a collection of finite-dimensional data vectors: $x(t) = q(\xi, t) - \bar{q}(\xi) \in \mathbb{R}^n$ where $t = t_1, t_2, ..., t_m$ [30]. $X(t)$ represents the varying component of the data vector with the time-averaged value $\bar{q}(\xi)$ removed [30]. The goal of POD is to find the optimal basis vectors in that we want to find vectors that be used to represent the flow field using the fewest number of modes [30], thus SVD is used.

1.6.3. Dynamic Mode Decomposition (DMD)

Dynamic mode decomposition (DMD) is a modal decomposition that allows for breaking up time-resolved data into modes [30]. DMD combines aspects of POD and discrete Fourier transform [7, 26, 30]. This results in mode structures that are not only spatiotemporally coherent but can be discerned solely from the data [30]. DMD at its heart is linear algebra, this method can be added upon and extended to several applications [30]. Since DMD is purely a data-driven algorithm in that it does not require governing equations, it has spanned several fields beyond fluid dynamics [30].

DMD is a relatively new technique in analyzing flow dynamics [26]. In DMD, the evolution of the flow field is approximated as a closed dynamical system [30], which can be approximated by an operator $\mathbf{A}$. The formulation of DMD, therefore, accounts for the temporal evolution of the DMD spatial modes ψ, the eigenvectors of the linear operator $\mathbf{A}$.

The snap-shot DMD methodology [30] is briefly introduced here. First, consider the time-dependent flow field in a collection of a N- sequence snapshot as follows:

$$\mathbf{V}^N = [v_1, v_2, \ldots, v_N] \tag{1.1}$$

Here the superscript N denotes the total number of flow field snapshots. The notation v_i denotes the i^{th} snapshot (time instance). Assuming that the time evolution of the flow field v can be describe by an operator $\mathbf{A}$ as:

$$v_{i+1} = \mathbf{A}v_i \tag{1.2}$$

Then $\mathbf{V}^N$ could be described using the first vector v_1 as:

$$\mathbf{V}^N = \mathbf{V}_1^N = [v_1, \mathbf{A}v_1, \ldots, \mathbf{A}^{N-1}v_1] \tag{1.3}$$

If the equation 1.2 holds true, the following equation could be obtained if the second vector v_2 is used:

$$\mathbf{A}\mathbf{V}_1^N = \mathbf{V}_2^N = \mathbf{V}_1^{N-1}\mathbf{S} + \mathbf{r}_{N-1}^T \tag{1.4}$$

where $\mathbf{r}$ is the residual vector, and $\mathbf{S}$ is the companion matrix, which contains some eigenvectors of $\mathbf{A}$. In practice, the DMD algorithm utilizes the Singular Value Decomposition to approximate the matrix $\mathbf{A}$. First, a SVD for the matrix $\mathbf{V}_1^{N-1}$ should be carried out as:

$$\mathbf{V}_1^{N-1} = \mathbf{U}\mathbf{\Sigma}\mathbf{W}^\star \tag{1.5}$$

where $\mathbf{U}$; Σ and $\mathbf{W}$ are the left singular vectors, singular values, and right singular vectors of the matrix $\mathbf{V}_1^{N-1}$, respectively. The notation $\star$ denotes the complex conjugate. A truncation rank r can be further selected from the diagonal of the matrix Σ out of the total number of the singular value $(N-1)$. Substituting the previous SVD into these equations and rearranging the resulting expression:

$$\tilde{\mathbf{U}_\mathbf{r}}^\star \mathbf{A} \tilde{\mathbf{U}_\mathbf{r}} = \tilde{\mathbf{U}_\mathbf{r}}^\star \mathbf{V}_2^N \tilde{\mathbf{W}_\mathbf{r}} \tilde{\mathbf{\Sigma}_\mathbf{r}}^{-1} \equiv \tilde{\mathbf{S}} \tag{1.6}$$

Solve the corresponding eigenvalue problem: $\tilde{\mathbf{S}}\mathbf{y_i} = \mu_i \mathbf{y_i}$ to find the eigenvalue i^{th} for matrix $\tilde{\mathbf{S}}$. Then the DMD modes ψ_i can be obtained as $\psi_i = \mathbf{U}\mathbf{y_i}$. The norm of each DMD mode represents the energy contribution of the mode to the evolution of flow field dynamics. The corresponding eigenvalues indicate the temporal evolution (mode frequency) of each mode. The temporal evolution of each mode can be found by computing its eigenvalue λ_i. Here, $\lambda_i = ln(\mu_i)/\Delta t$. The real part of λ_i $(Re(\lambda_i))$ stands for the growth rate of the DMD modes ψ_i. Its complex part $(\Im(\lambda_i)/2\pi)$ represents the frequency of ψ_i. Δt is the time step between two successively snapshots.

1.7. Summary

In this work, we use Direct Numerical Simulation to simulate blood flow dynamics in the human brain without any assumption on the turbulent modeling. Using our results from these

simulations, we hope to create a better risk factor analysis calculation method of whether or not an aneurysm in a patient will rupture, is close to rupturing, or poses no immediate risks to the patient. This report in turn can help narrow surgeons decide on the best treatment for a specific patient. The details of our methodology in the next chapter.

2. METHODOLOGY

2.1. Anatomical models

In this work, all aneurysm models are taken from the Aneurisk project `https://github.com/permfl/AneuriskData`. All models are downloaded from the Aneurisk project. Before any simulations can be run, we need to calculate the volumetric space of our medium i.e. the volume of each aneurysm as well as the volume of the parent artery to, the artery to which the aneurysm is attached to. This was done in the three-dimensional modeling program, Paraview by opening each aneurysm STL file and measuring the diameter of the aneurysm, the diameter of the vessel, and the height of the aneurysm with the rule tool. Each dimension was measured several times to minimize user error. Table 3.1 shows the calculated average diameter for each artery and each aneurysm as well as the calculated average height of each aneurysm. Now that we have the dimensions of our medium we can move on to modeling blood flow.

Table 2.1. Measured dimensions for eleven selected aneurysm models from the Aneurisk project (`https://github.com/permfl/AneuriskData`). These dimensions were calculated in Paraview and verified using the dimensions from the Aneurisk data.

Patient ID	Artery Diameter (D)	Aneurysm Diameter (W)	Aneurysm Height (H)	Location
C0002	3.6275 mm	4.3725 mm	7.7625 mm	L-ICA
C0006	3.2625 mm	7.9025 mm	4.8431 mm	ICA
C0014	4.5875 mm	6.9175 mm	5.2375 mm	ICA
C0016	3.0825 mm	7.7675 mm	7.4925 mm	ICA
C0034	3.0766 mm	8.5366 mm	7.6166 mm	ICA
C0036	3.9625 mm	10.7725 mm	14.2625 mm	ICA
C0042	3.9425 mm	8.4375 mm	7.7575 mm	ICA
C0067	3.5375 mm	4.1125 mm	3.0875 mm	ICA
C0075	3.5725 mm	12.0225 mm	11.8025 mm	ICA
C0085	3.3275 mm	9.6025 mm	7.1475 mm	ICA
C0088b	3.4625 mm	7.3125 mm	7.2875 mm	ICA

2.2. Extracting a 3D Model From Patient Data

Before anything else can be done, an aneurysm model needs to be generated, done via segmentation. Segmentation is extracting vessels from image data so that a 3D model can be created. [24]. The segmentation process depends on image quality and precision. [24]. Better quality leads

to clear models while precision leads to more accurate models. The image size is another factor. The size of the image voxels determines the approximated smoothness of rectangular voxels. [24]. When 3D geometries are generated, the region of interest, then can the mesh be created.

We used Slicer for this research project, as Slicer is an easy-to-use three-dimensional modeling software with the ability to extract a 3D model from a Digital Imaging and Communications in Medicine (DICOM) file part. In Slicer, the DICOM folder directory is imported using the DICOM Module These DICOM files are loaded into the local Slicer DICOM database automatically. The Slicer DICOM database organizes the DICOM file parts by Patient id making it easier to load file parts from a single patient. Once the database is generated, DICOM files can be loaded by the Patient or as individual file parts.

Once the Slicer DICOM database is all set up, then can come the actual segmentation process. To create a segment from a DICOM file part, Slicer switched to the segmentation module. From here new segment was created from the desired DICOM file part, either a CT or MRI scan or another three-plane representation. These three planes are crucial to generate a 3D model otherwise you get a flat 2D plane. After the segment is created, Slicer is switched to the segmentation editor module. In the segmentation module, several filters can be applied to extract the Circle of Willis (COW) from the DICOM file part. For this, the threshold filter was determined to get the best results. The threshold filter works by using the brightness intensity of the image to extract the model. Occasionally, the slider bar had to be adjusted so that the intensity range for the threshold filter extracts the correct parts.

The next step is to export the model as a stereolithography (STL) file and clean up the model. The segmentation module at the bottom has the option to export the model as an STL. At this point, the final model has not yet been achieved as the threshold filter can only do so much. From here there are a few more steps before the final model can be realized and ready for simulation. For the cleaning, another 3D modeling software was used, Meshmixer. First, the STL file was imported into Meshmixer. Second, a random spot on the COW was selected and extended to all other connected parts via the selection editor. Next, the selection was inverted to isolate all unnecessary parts in the model and then, was deleted.

At this point, each patient's COW has been realized, however, the aneurysms from each still need to be extracted. The COWs were exported as STL files for later use. The next step is to

isolate the aneurysm for each patient's COW. This requires the model to be edited as some parts of the model are cut away. Several plane cuts were made in the model of each patient's COW to crop around the volume of each aneurysm in question. Finally, each aneurysm model was exported as an STL file.

2.3. Computational Setup

For each of the eleven cases listed, each aneurysm was extracted from its respective .stl file and cleaned up in Meshmixer. The extraction process is mentioned in more detail in the previous subsection. After the extraction of each aneurysm, in Meshmixer the inlet and outlet portion of the aneurysm's patient artery were extended for consistency purposes.

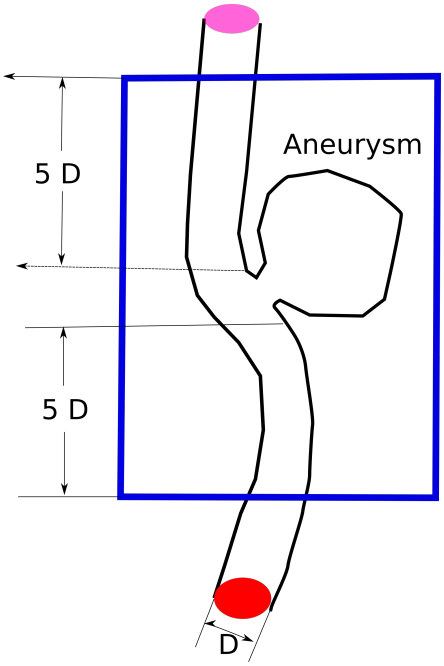

Figure 2.1. Illustration of a y-plane view of a sample fluid mesh. This illustration shows the fluid mesh setup for each aneurysm as previously mentioned where D represents the diameter of the parent artery and the blue outline is the bounds of the fluid mesh.

After which, each aneurysm was imported in Pointwise so the fluid meshes could be created. It should also be noted that in our simulation negative y points toward the heart and positive y points away from the heart. Each fluid mesh was created with a rectangular prism encapsulating their respective aneurysm. The constraints of the fluid meshes are as follows, along the x and z-axes the fluid mesh's corresponding aneurysm was fully enclosed then along the y-axis the negative

edge was placed at about five times the diameter the of parent artery from the boundaries of the aneurysm while the positive edge along the y-axis was placed at about five times the diameter the of parent artery from the boundaries of the aneurysm or before the end of the outlet whichever was less. This is best illustrated by the following figure 2.1. The precision of the mesh was set to 201 voxels along both the x- and z-axes and 321 voxels along the y-axis for a total of 12.9 million points. The extended models of each aneurysm are shown in Figure 2.2.

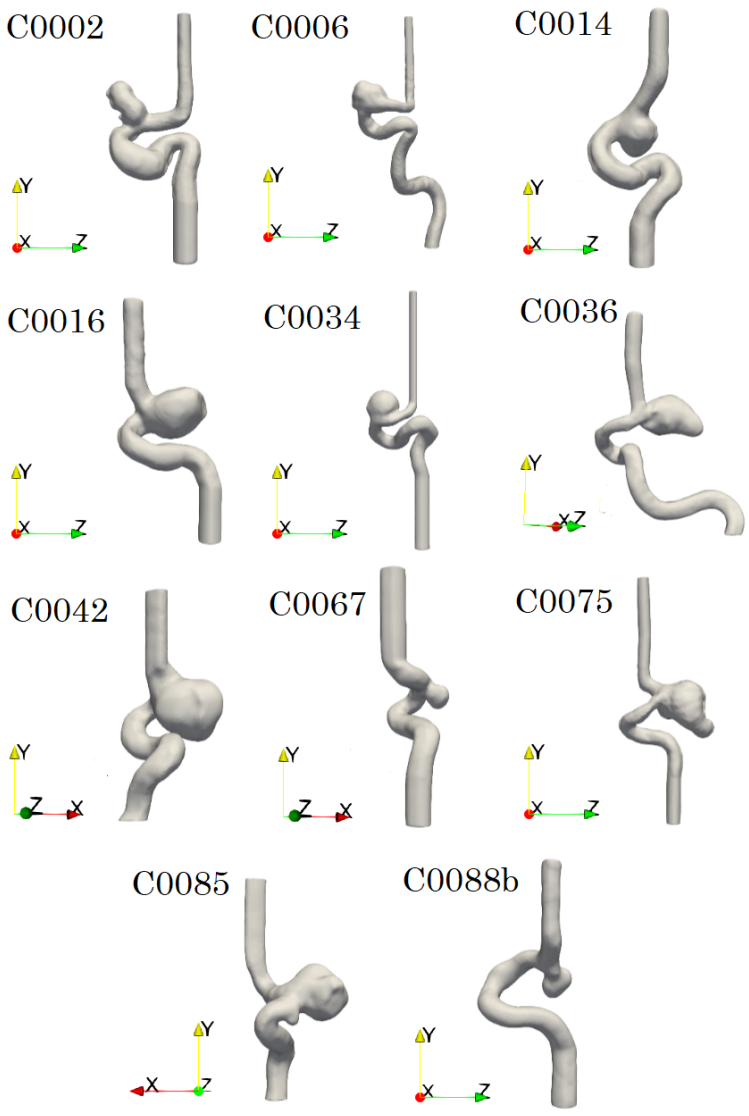

Figure 2.2. Extracted aneurysms listed as follows: top row (from left to right), C0002, C0006, and C0014; second row (from left to right), C0016, C0034, and C0036; third row (from left to right), C0042, C0067, and C0075; bottom row (from left to right), C0085 and C0088b.

2.4. Numerical simulations of blood flow dynamics

The numerical method employed in this work has been extensively described and thoroughly validated against *in vitro* [15] and *in vivo* data [18]. Therefore, only a brief description of the numerical method is presented in this section. For more details about the method the reader is referred to the previous publications: [14, 15, 19]. The governing equations for the fluid (blood) are the three-dimensional, unsteady incompressible continuity and Navier-Stokes equations [17]. The governing equations are solved in a background curvilinear domain that contains the complex geometry of the intracranial aneurysm model using the sharp-interface curvilinear-immersed boundary (CURVIB) method [14]. The discrete equations are integrated in time using a fractional step method [11]. A Newton-Krylov solver is used to solve the momentum equations in the momentum step and a Generalized Minimal Residual (GMRES) solver with a multigrid preconditioner is employed for the Poisson equation [16].

At the inflow boundary, a uniform velocity profile varying in time is prescribed with the peak velocity of $U_0 = 0.5m/s$ using the measurement data at the Internal Carotid Artery of a human subject [6]. The inlet locates approximately $5D_0$ far from the sac. Here D_0 is the diameter of the inlet. At the outflow boundary, Neumann-type boundary conditions are specified for the velocity components. No-slip and no-flux conditions are prescribed at all artery wall boundaries, which are considered rigid.

The resulting parameters for the simulations are as follows:

$$Re = \frac{U_0 L}{\nu} = \frac{0.5m/s \times 10^{-3}m}{3.35 \times 10^{-6}m^2/s} \approx 150. \tag{2.1}$$

The cardiac cycle is chosen at $T = 72pbm = 60seconds/72 = 0.83seconds$. The non-dimensional timescale is thus:

$$\tau = \frac{D}{U_0} = \frac{1 \times 10^{-3}}{0.5} = 2 \times 10^{-3}seconds \tag{2.2}$$

With the discretization of 4000 timesteps per cardiac cycle, this amount to the physical timestep of:

$$\Delta t = 0.83seconds/4000 \approx 0.21 \times 10^{-3}seconds \tag{2.3}$$

Set this into the control.dat, which corresponds to the non-dimensional timestep of:

$$dt = \frac{\Delta t}{\tau} = \frac{0.21 \times 10^{-3} seconds}{2 \times 10^{-3} seconds} = 0.10375 \tag{2.4}$$

Table 2.2. The computational cases for all models. The size of the structural grid is indicated in the i, j, k directions.

Patient ID	Simulation Progress	DMD Progress	Writing	Grid Size
C0002	Complete	Complete	Complete	$201 \times 201 \times 321$
C0006	Complete	Complete	Complete	$201 \times 201 \times 321$
C0014	Complete	Complete	Complete	$201 \times 201 \times 321$
C0016	Complete	Complete	Complete	$201 \times 201 \times 321$
C0034	Complete	Complete	Complete	$201 \times 201 \times 321$
C0036	Complete	Complete	Complete	$201 \times 201 \times 321$
C0042	Complete	Complete	Complete	$201 \times 201 \times 321$
C0067	Complete	Complete	Complete	$201 \times 201 \times 321$
C0075	Complete	Complete	Complete	$201 \times 201 \times 321$
C0085	Complete	Complete	Complete	$201 \times 201 \times 321$
C0088b	Complete	Complete	Complete	$201 \times 201 \times 321$

2.5. DMD analysis procedure

The following cases are of interest for DMD analysis from the Aneurisk project: 1) C0002; 2) C0006; 3) C0014; 4) C0016; 5) C0034; 6) C0036; 7) C0042; 8) C0067; 9) C0075; 10) C0085. First, an analysis of blood flows in brain aneurysms using CFD is carried out. After that, the capability of DMD to identify the incoming jet and classify the incoming jet is implemented in the following steps:

- Step 1: First, one cardiac cycle is discretized into 4000 timesteps. A total of 12,000 timesteps (3 cardiac cycles) of simulations are performed for one case. The timesteps from 8,000 to 12,000 (the last cycle) are selected for DMD analysis. The spacing between two successive instances of DMD is $\Delta t = 100$ timesteps (40 instances for one DMD analysis). Compare the incoming jet, which needs to show the velocity distribution in a plane at the timestep 9,000 and 9500 for all cases.

- Step 2: Recover the physical velocities by multiplying the velocity vectors in Paraview with a factor of $U_0 = 0.5m/s$. After this step, the physical velocities are correctly reflected in the Paraview results.

- Step 3: Cut the aneurysm domain. Select the region k value so that it contains only the aneurysm. Adjust the i and j directions so that only the aneurysm dome is included in the final data.

- Step 4: Run the Matlab code using the PBS script (not on the GUI).

- Step 5: To visualize the modes using Red (Mode 1), Green (Mode 2), and Blue (Mode 3) in Paraview.

For each patient, the aneurysm mesh was kept with no down-scaling and the data cells were written to .csv files. This was done by importing each of the aneurysms in Paraview. Secondly, for each case, the aneurysm was isolated as much as possible trimming the ends of the parent artery as shown in Figure 2.3. At this point, any part of the parent artery floating in free space, circled in red in Figure 2.3, can be ignored for now as clipping this off now can run into errors when Matlab tries to read the .csv files.

Once the aneurysm has been isolated then the model can be exported as a list of .csv files, one for each timestep. Next, the DMD code was run on the .csv files to get the DMD modes. Due to the large size of several .csv files, some upwards of approximately 10 GB, the DMD Matlab code was run on the NDSU CCAST High-Performance Computing server.

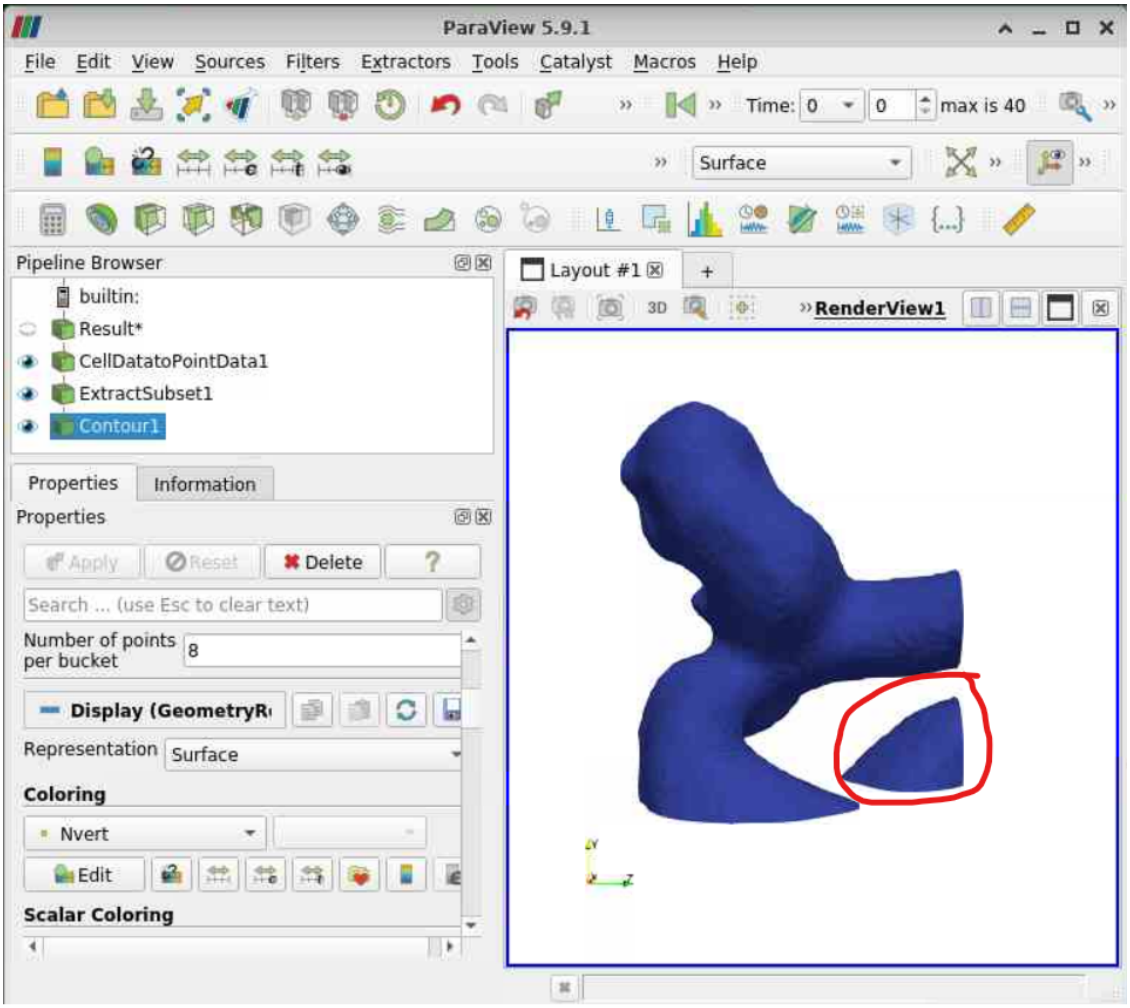

Figure 2.3. Visualization of the DMD setup in Paraview. Here is shown the extracted subset of C0002's aneurysm.

2.6. The MATLAB code for DMD analysis

`Assemble_Data.m`

```
function [X coord_x coord_y coord_z ] = Assemble_Data()
    Number_Of_Instances = 40;

    X = [];

    for my_time = 1: Number_Of_Instances
    filename = sprintf('data06x_%d.csv',my_time-1);
    loading_file = readmatrix(filename);

    % Compute velocity magnitude
```

```
        % Vec_X 6
        % Vec_Y 7
        % Vec_Z 8

        Vec  = [];
        Vec  = [loading_file(:,6); loading_file(:,7); loading_file(:,8)];
        %Vec  = sqrt(loading_file(:,6).^2 + loading_file(:,7).^2 +
             loading_file(:,8).^2);

        X = [X Vec];

        if (my_time == 1)
             coord_x = loading_file(:,3);
             coord_y = loading_file(:,4);
             coord_z = loading_file(:,5);
        end

    end
```

mrDMD.m

```
    function tree = mrDMD(Xraw, dt, r, max_cyc, L)
    % function tree = mrDMD(Xraw, dt, r, max_cyc, L)

    % Inputs:
    % Xraw       n by m matrix of raw data,
    %            n measurements, m snapshots
    % dt         time step of sampling
    % r          rank of truncation
    % max_cyc    to determine rho, the freq cutoff, compute
    %            oscillations of max_cyc in the time window
    % L          number of levels remaining in the recursion

    T = size(Xraw, 2) * dt;
    rho = max_cyc/T; % high freq cutoff at this level
    sub = ceil(1/rho/8/pi/dt); % 4x Nyquist for rho

    %% DMD at this level
    Xaug = Xraw(:, 1:sub:end); % subsample
    Xaug = [Xaug(:, 1:end-1); Xaug(:, 2:end)];
    X = Xaug(:, 1:end-1);
    Xp = Xaug(:, 2:end);
```

```
[U, S, V] = svd(X, 'econ');
r = min(size(U,2), r);
U_r = U(:, 1:r); % rank truncation
S_r = S(1:r, 1:r);
V_r = V(:, 1:r);

Atilde = U_r' * Xp * V_r / S_r;
[W, D] = eig(Atilde);
lambda = diag(D);
Phi = Xp * V(:,1:r) / S(1:r,1:r) * W;

%% compute power of modes
Vand = zeros(r, size(X, 2)); % Vandermonde matrix
for k = 1:size(X, 2),
    Vand(:, k) = lambda.^(k-1);
end;

% the next 5 lines follow Jovanovic et al, 2014 code:
G = S_r * V_r';
P = (W'*W).*conj(Vand*Vand');
q = conj(diag(Vand*G'*W));
Pl = chol(P,'lower');
b = (Pl')\(Pl\q); % Optimal vector of amplitudes b

%% Reconstruct the modes
%% Psi = diag(b)*Vand;

%% Reconstruct the data ---> Needs future works here !!
%%X_reconstruct = Phi * Psi;

%% consolidate slow modes, where abs(omega) < rho
omega = log(lambda)/sub/dt/2/pi;
mymodes = find(abs(omega) <= rho);

thislevel.T = T;
thislevel.rho = rho;
thislevel.hit = numel(mymodes) > 0;
thislevel.omega = omega(mymodes);
thislevel.P = abs(b(mymodes));
thislevel.Phi = Phi(:, mymodes);
thislevel.sigma = diag(S);
thislevel.lambda = lambda;
```

```
    thislevel.b  = b;
    %%thislevel.Psi = Psi;

    %% recurse on halves
    if L > 1,
        sep = floor(size(Xraw,2)/2);
        nextlevel1 = mrDMD(Xraw(:, 1:sep),dt, r, max_cyc, L-1);
        nextlevel2 = mrDMD(Xraw(:, sep+1:end),dt, r, max_cyc, L-1);
    else
        nextlleve1 = cell(0);
        nextlevel2 = cell(0);
    end;

    %% reconcile indexing on output
    % (because Matlab does not support recursive data structures)
    tree = cell(L, 2^(L-1));
    tree{1,1} = thislevel;

    for l = 2:L,
        col = 1;
        for j = 1:2^(l-2),
            tree{l, col} = nextlevel1{l-1, j};
            col = col + 1;
        end;
        for j = 1:2^(l-2)
            tree{l, col} = nextlevel2{l-1, j};
            col = col + 1;
        end;
    end;
```

mrDMD_map.m

```
    function [map, low_f_cutoff] = mrDMD_map(mrdmd)
    % function [map, low_f_cutoff] = mrDMD_map(mrdmd)

    [levels, M] = size(mrdmd);

    map = zeros(levels, M);

    low_f_cutoff = zeros(levels+1, 1);
    for i = 1:levels,
        chunks = 2^(i-1);
        K = M / chunks;
```

```
        for j = 1:chunks,
            f = abs(imag(mrdmd{i, j}.omega));
            P = mrdmd{i, j}.P;

            P = P(f >= low_f_cutoff(i));
            if ~isempty(P),
                map(i, (1:K)+(j-1)*K) = mean(P);
            end;
        end;

        low_f_cutoff(i+1) = mrdmd{i,1}.rho;
    end;
```

Show_Map_Frequency.m

```
    % Assemble the data
    [X coord_x coord_y coord_z ] = Assemble_Data();

    % size of the grid in Paraview
    % these numbers are not the same for every case
    nx = 101;
    ny = 101;
    nz = 101;

    dt = 0.857; % seconds
    L = 2; % number of levels
    r = 4; % rank of truncation
    T = 0.857; % seconds
    max_cycle  = 200; % cutoff-frequency
    mrdmd = mrDMD(X, dt, r,  max_cycle, L);

    % compile visualization of multires mode amplitudes
    [map, low_f] = mrDMD_map(mrdmd);
    [L, J] =size(mrdmd);

    % Save the analysis
    save('Analysis_Results.mat','mrdmd','L','r','T','dt','map','J','low_f','coord_x','coord_y',
        'coord_z','-v7.3'); % Note the -v7.3 is for files larger than 2GB

    %%
    % figure;
    % imagesc(-map);
    % set(gca, 'YTick', 0.5:(L+0.5), 'YTickLabel', floor(low_f*10)/10);
```

```
% set(gca, 'XTick', J/T*(0:T) + 0.5);
% set(gca, 'XTickLabel', (get(gca, 'XTick')-0.5)/J*T);
% axis xy;
% xlabel('Time (sec)');
% ylabel('Freq. (Hz)');
% colormap pink;
% grid on;

% Check if the result folder is there
if not(isfolder('VTK_Files'))
    mkdir('VTK_Files')
else
    delete('./VTK_Files/*.*');
end

%% Export the modes out
for level= 1: L
    Number_Of_Bin = 2.^(level -1);
    for bin=1:Number_Of_Bin
        Current_Cell = mrdmd{level,bin};
        omega = Current_Cell.omega;
        number_of_modes = size(omega,1);

        Spectrum{level,bin}.omega  = Current_Cell.omega;
        Spectrum{level,bin}.power  = Current_Cell.P;
        Spectrum{level,bin}.sigma  = Current_Cell.sigma;
        Spectrum{level,bin}.lambda = Current_Cell.lambda;
        Spectrum{level,bin}.b      = Current_Cell.b;

        for k=1:number_of_modes % plot first four DMD modes
            filename = sprintf('VTK_Files/DMD_Mode_nf%d_b%d_l%d.vtk',k,bin,level);
            Phi  = Current_Cell.Phi;
            mymode = Phi(:,k);
            my_size = length(mymode)/2;

            %% == Taking the velocity vectors out #
            current_mode = mymode(1:my_size);
            n_points = length(coord_x);
            U_x = current_mode(1:n_points);
            U_y = current_mode(n_points+1:2*n_points);
            U_z = current_mode(2*n_points+1:end);
```

```
            Velocity_x = reshape(U_x, nx, ny, nz);
            Velocity_y = reshape(U_y, nx, ny, nz);
            Velocity_z = reshape(U_z, nx, ny, nz);

            Umag = sqrt(Velocity_x.^2  +Velocity_y.^2 + Velocity_z.^2);
            x = reshape(coord_x, nx, ny, nz);
            y = reshape(coord_y, nx, ny, nz);
            z = reshape(coord_z, nx, ny, nz);

            Write_To_VTK(filename, x, y, z,Velocity_x, Velocity_y, Velocity_z);

        end % End of individual mode
    end % End of bin
end % End of level


% Save the power spectrum separately so that it is easier to take out
save('Spectrum.mat','Spectrum','-v7.3'); % Note the -v7.3 is for files larger than 2GB

% % For debug
% lamda_k = Spectrum{1,1}.lambda;
% theta = 0:2*pi/100:2*pi;
% my_x = cos(theta);
% my_y = sin(theta);

% figure(2);
% plot(my_x, my_y);
% hold on
% plot(real(lamda_k),imag(lamda_k),'r o')
% axis equal

% number_of_instances = size(X,2);
%
% myb = Spectrum{1,1}.b;
%
%
% %% compute power of modes
% Vand = zeros(r, number_of_instances); % Vandermonde matrix
% for k = 1:number_of_instances
%     Vand(:, k) = lamda_k.^(k-1);
% end;
%
```

```
% time_dynamics = diag(myb) * Vand;
%
% % Compute power for each mode
% Power_Scale = abs(myb.*lamda_k.^number_of_instances);
% [B Index] = sort(Power_Scale,'descend');
%
% figure;
% for i = 2:2:16 % Ignore the first mode  - the mean
% dyna_mode = time_dynamics(Index(i),:);
% hold on
% plot(imag(dyna_mode));
% end
%
```

Write_To_VTK.m

```
function Write_To_VTK(filename, x, y, z, u, v, w)
%Output file name

nr_of_elements=numel(x);
fid = fopen(filename, 'w');

%ASCII file header
fprintf(fid, '# vtk DataFile Version 3.0\n');
fprintf(fid, 'VTK from Matlab\n');
fprintf(fid, 'BINARY\n\n');
fprintf(fid, 'DATASET STRUCTURED_GRID\n');
fprintf(fid, ['DIMENSIONS ' num2str(size(x,1)) ' ' num2str(size(x,2)) ' '
    num2str(size(x,3)) '\n']);
fprintf(fid, ['POINTS ' num2str(nr_of_elements) ' float\n']);
fclose(fid);

%append binary x,y,z data
fid = fopen(filename, 'a');
fwrite(fid, [reshape(x,1,nr_of_elements);
reshape(y,1,nr_of_elements);
reshape(z,1,nr_of_elements)],'float','b');

%append another ASCII sub header
fprintf(fid, ['\nPOINT_DATA ' num2str(nr_of_elements) '\n']);
fprintf(fid, 'VECTORS velocity_vectors float\n');

%append binary u,v,w data
```

```
fwrite(fid, [reshape(u,1,nr_of_elements);
reshape(v,1,nr_of_elements);
reshape(w,1,nr_of_elements)],'float','b');

%append some scalar data
fprintf(fid, '\nSCALARS Umag float\n'); %ASCII header
fprintf(fid, 'LOOKUP_TABLE default\n'); %ASCII header
fwrite (fid, reshape(sqrt(u.^2+v.^2+w.^2),1,nr_of_elements),'float','b'); %binary data

fclose(fid);
```

3. RESULTS

3.1. Model validation: Simulation of a model for axisymmetric stenosed vessel

To validate our methodology, we first perform CFD simulation in an idealized model of a stenosis artery. Stenosis is the narrowing of walls in blood vessels caused by plaque build-up or increased stress on the vessel walls. [31]. The narrowing of the blood vessels makes them more prone to rupturing as well as disrupting the overall flow of blood. [31]. There are two types of stenosed geometries, axisymmetric and eccentric stenosis. [31]. In axisymmetric stenosis, the blood flow toward the center of the vessel, whereas in eccentric stenosis, blood flows toward one of the sides of the vessel. [31]. Our simulation results agree well with the reported dynamics in stenosis literature.

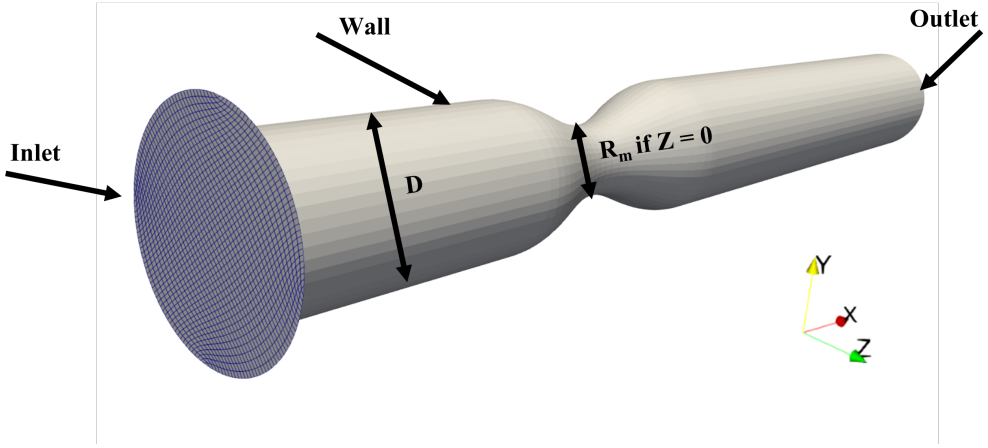

Figure 3.1. Mesh of Stenosed vessel.

Here the axisymmetric stenosis model is represented as:

$$\frac{R_m(Z)}{D} = 0.5 - 0.125[1 + \cos(\pi Z/D)] : -D \leq Z \leq D \tag{3.1}$$

where Z = 0 is the throat of the stenosis. D is the unobstructed tube diameter and R_m is the local radius that varies with axial direction Z [31]. Figure 3.1 provides the mesh for this model.

Using large eddy simulation we reconstructed the axisymmetric stenosed vessel simulation Tan et al generated in their paper. In correspondence with Tan et al's paper, in our simulation, shown in figure 3.2, the Reynolds number was 1000 with a vessel diameter of 1 cm and a stenosis diameter of 0.5 cm. Our mesh voxel dimensions were $201 \times 201 \times 231$ for a total of 9.3 million points.

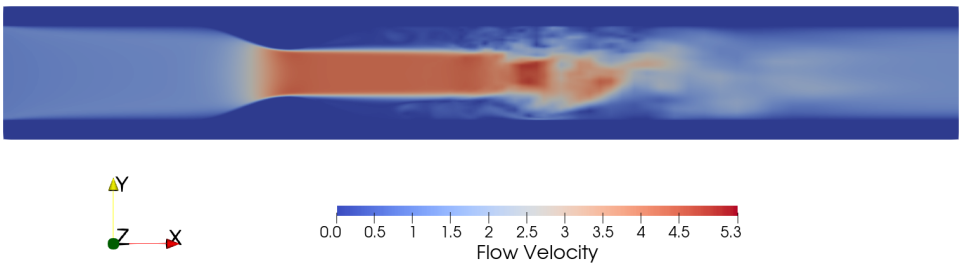

Figure 3.2. Animation Still shot of CFD model of blood flow in an Axisymmetric Stenosed Vessel

Figure 3.3, shows this simulation as velocity streamlines of the blood flow. A slice of the inlet was down-sampled to show the mesh grid.

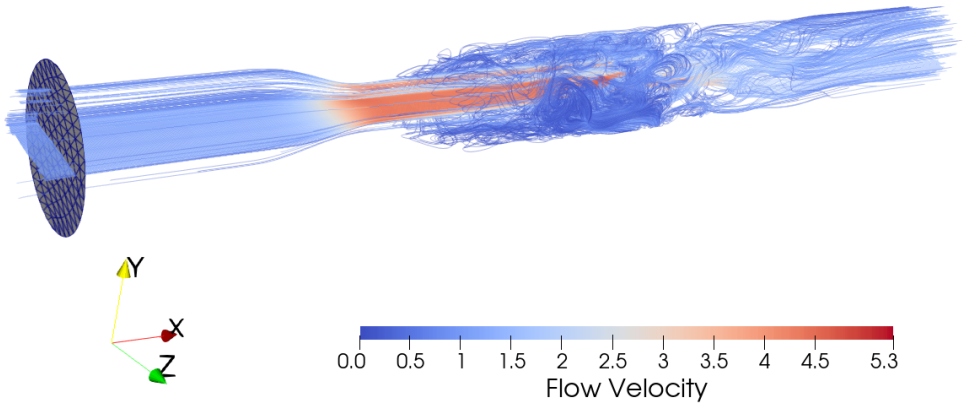

Figure 3.3. Animation Still shot of CFD model of blood flow showing flow velocity streamlines in an Axisymmetric Stenosed Vessel.

3.2. Blood flow structures in the aneurysm models

3.2.1. Two-dimensional flow patterns on representative planes

The Computational Fluid Dynamics simulations have demonstrated that the hemodynamic conditions inside the aneurysms are dominated by its inflow jet [15]. A slice was taken of each model to show the hemodynamic conditions of the aneurysms. This was done in Paraview by taking a plane cut of each and then saving the fluid flow animation frames; ten frames of the fluid flow were sampled from 40 total frames.

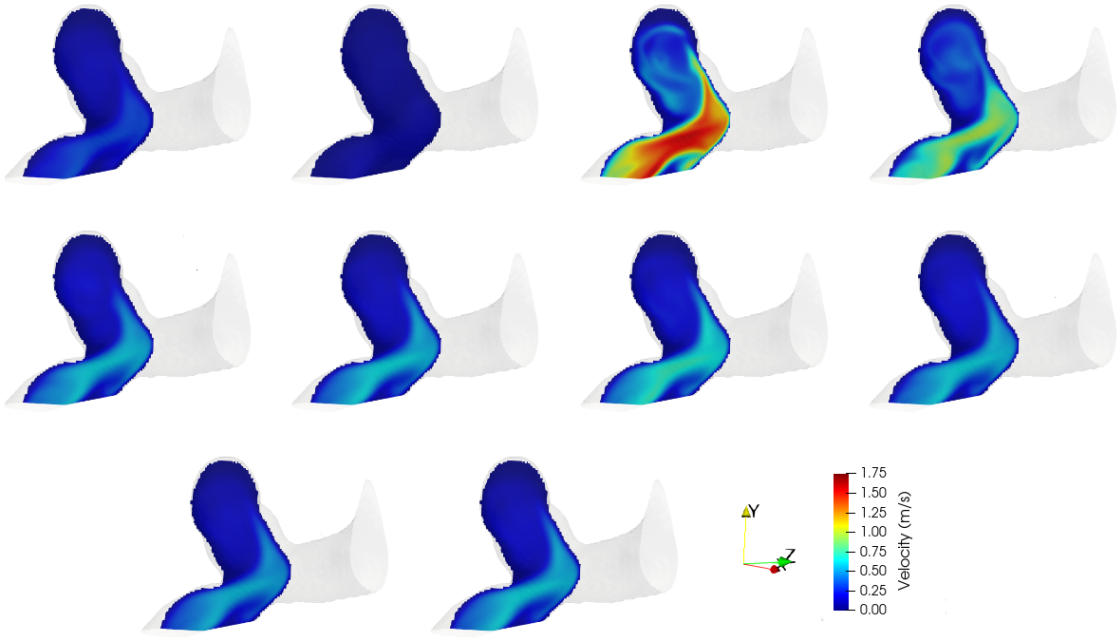

Figure 3.4. C0002 Flow Velocity xz-plane slice at timesteps (from left to right) 8200, 8600, 9000, 9400, 9800, 10200, 10600, 11000, 11400, and 11800; where 9000 is the time of peak velocity.

In patient C0002's aneurysm, blood fills up the aneurysm, but it appears to lose momentum as the inflow jet collides with the aneurysm wall as seen in Figure 3.4. This loss in momentum is most likely due to the oblong shape of this aneurysm. The shape of C0002's aneurysm makes it unique in that unlike the other aneurysms in the report, it doesn't have the expected ellipsoid shape. Its oblong shape is most likely due to where the inflow jet collides with the aneurysm wall.

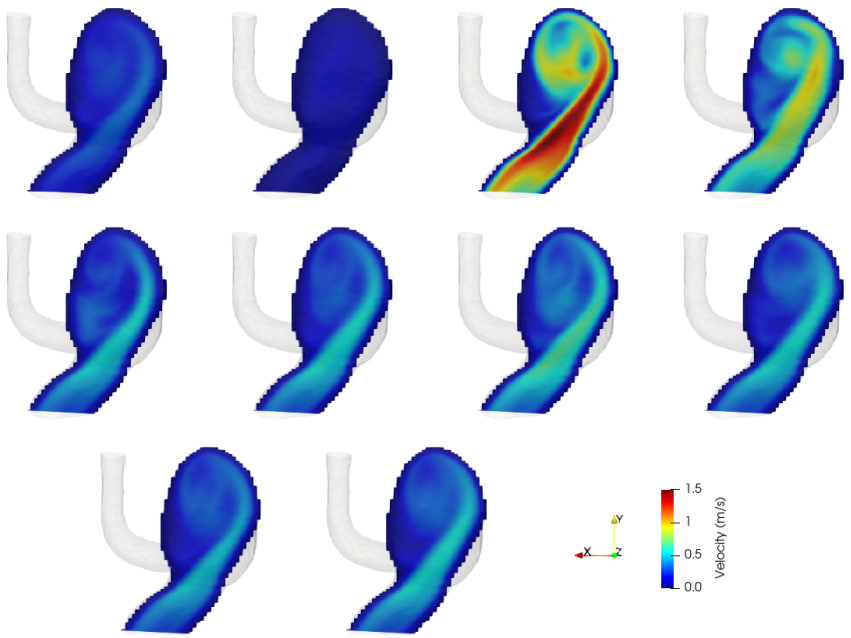

Figure 3.5. C0006 Flow Velocity z-plane slice at timesteps (from left to right) 8200, 8600, 9000, 9400, 9800, 10200, 10600, 11000, 11400, and 11800; where 9000 is the time of peak velocity.

Blood in patient C0006's aneurysm fills up the aneurysm flowing in a whirlpool-like motion before exiting and continuing on as seen in Figure 3.5. The flow velocity of blood at the outlet is greater than at the inlet due to the circular momentum built up in the aneurysm. Unlike C0002, this aneurysm has a more ellipsoid shape and has higher flow velocity, especially at timestep 9000 (ts = 9000). Additionally, it is worth noting that C0006's aneurysm is approximately the same size as C0002's aneurysm according to the collected measurements.

In patient C0014's aneurysm (Figure 3.6), we can see a similar whirlpool-like motion. Unlike C0006's aneurysm, the blood flow velocity here is less and decays faster. This might be due to the fact of where the inflow jet hits the aneurysm wall, hitting it fairly close to the outflow jet. Something that is also worth noting is that this aneurysm's parent artery diameter is the largest in comparison to the other cases.

In patient C0016's aneurysm (Figure 3.7), the blood flow pattern is not defined as any of the other previously mentioned aneurysms. However, there seems to be an overall circular motion. This circular motion is better conveyed by the DMD modes for this aneurysm as shown in Figure 3.29. Another characteristic that differentiates this aneurysm from all the others the blood flow seems a

lot more erratic as seen in Figure 3.7. This erratic flow pattern is probably due to the orientation of the aneurysm and where the inflow jet hits the aneurysm wall.

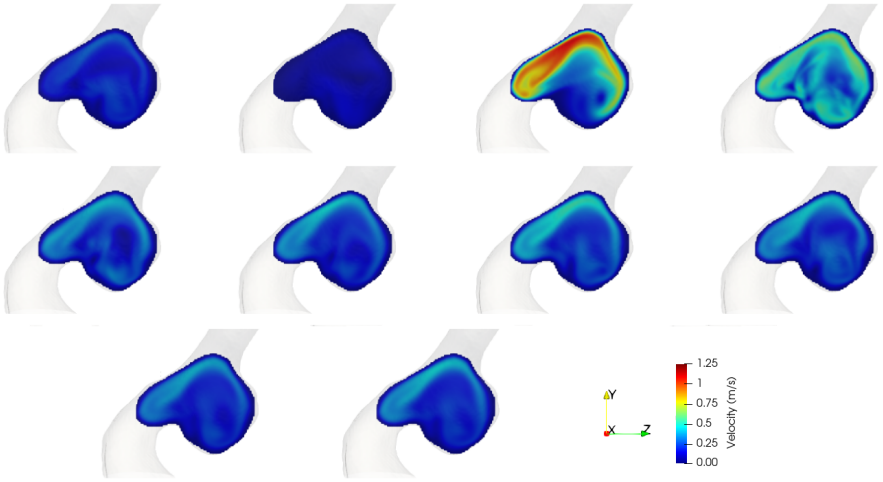

Figure 3.6. C0014 Flow Velocity z-plane slice at timesteps (from left to right) 8200, 8600, 9000, 9400, 9800, 10200, 10600, 11000, 11400, and 11800; where 9000 is the time of peak velocity.

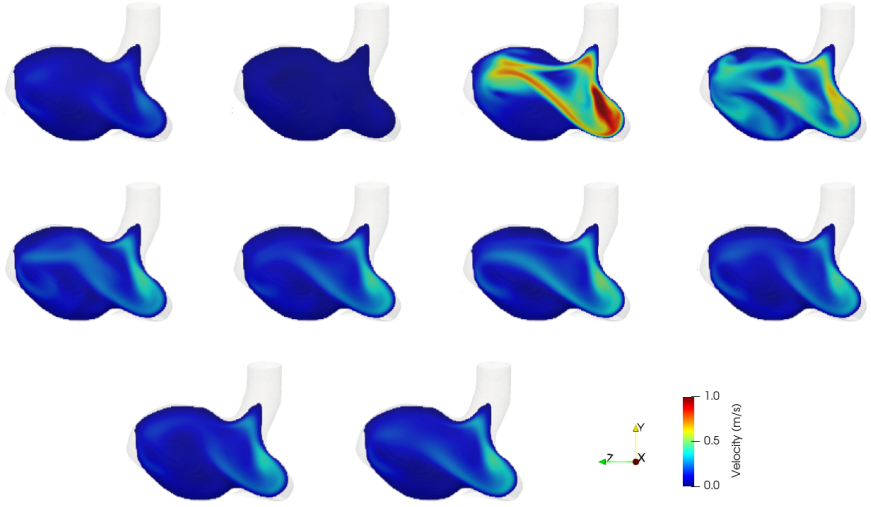

Figure 3.7. C0016 Flow Velocity x-plane slice at timesteps (from left to right) 8200, 8600, 9000, 9400, 9800, 10200, 10600, 11000, 11400, and 11800; where 9000 is the time of peak velocity.

Like with patients C0006 and C0016, blood in patient C0034's aneurysm fills up the aneurysm flowing in a whirlpool-like motion before exiting and continuing on. Similarly, the flow velocity of blood at the outlet is greater than at the inlet due to the circular momentum built up in the aneurysm. This whirlpool-like motion appears to be more apparent in this case than in C0006. Additionally, it is worth noting that C0034's aneurysm is approximately the same height as c0002's aneurysm height and has approximately the same diameter as C0006's aneurysm according to the collected measurements. This doesn't come as much of a surprise as c0034's aneurysm is nearly twice the size of c0002's aneurysm and c0006's aneurysm respectively.

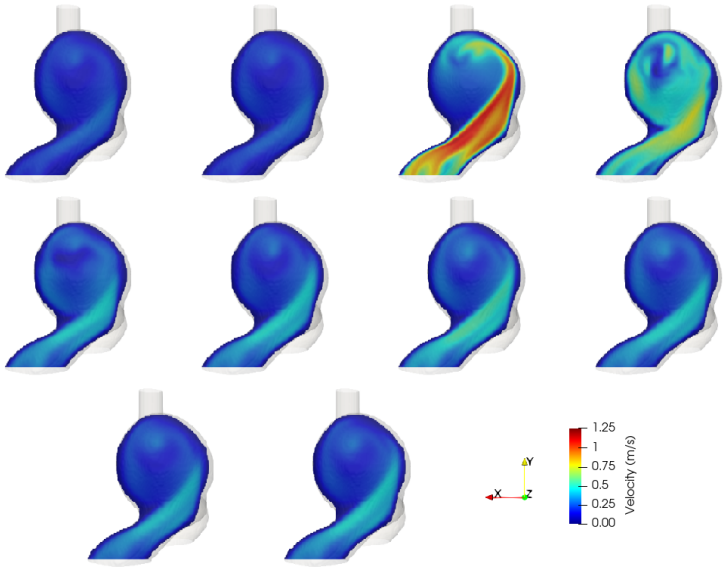

Figure 3.8. C0034 Flow Velocity z-plane slice at timesteps (from left to right) 8200, 8600, 9000, 9400, 9800, 10200, 10600, 11000, 11400, and 11800; where 9000 is the time of peak velocity.

Unlike many of the previous cases, the flow in C0036 takes more of a corkscrew path, spiraling the distal wall of the aneurysm and losing momentum as can be seen in Figure 3.9. The inflow jet hits the very edge of the aneurysm wall where it meets the edge of the parent artery wall. It is also worth mentioning that this aneurysm is essentially tied for the largest aneurysm by volume with C0075's aneurysm mentioned later in this paper.

In patient C0042's aneurysm, it may not be as clear as in the previous cases, but the whirlpool motion is still there. This particular circumstance is most likely because of where the inflow jet impinges on the aneurysm wall as can be seen in Figure 3.10. Due to where the inflow jet

hits the aneurysm wall, the momentum of the flow that should be conserved within the aneurysm is lost to flow leak out to the parent artery near the aneurysm's outflow jet. It is also worth noting that this aneurysm is the third largest by volume in comparison to the other cases.

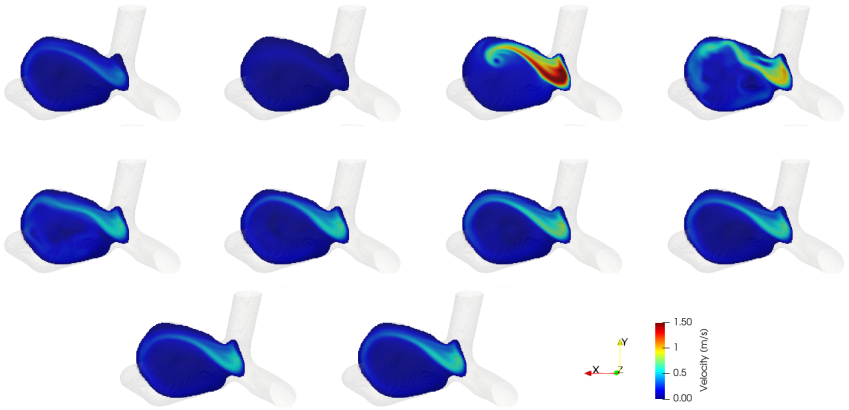

Figure 3.9. C0036 Flow Velocity z-plane slice at timesteps (from left to right) 8200, 8600, 9000, 9400, 9800, 10200, 10600, 11000, 11400, and 11800; where 9000 is the time of peak velocity.

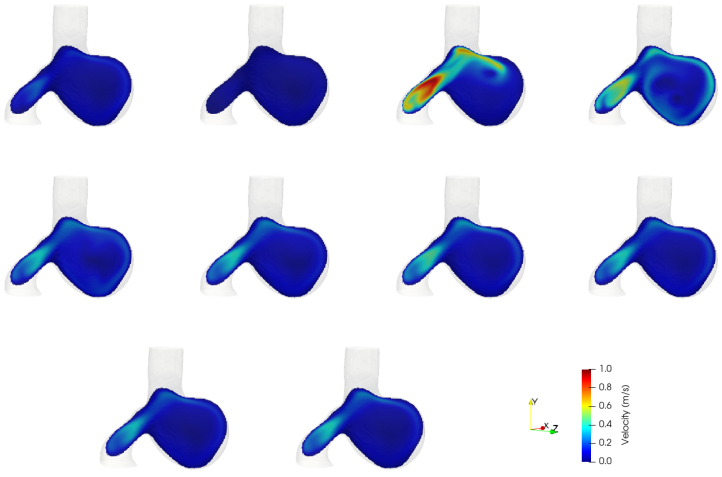

Figure 3.10. C0042 Flow Velocity xz-plane slice at timesteps (from left to right) 8200, 8600, 9000, 9400, 9800, 10200, 10600, 11000, 11400, and 11800; where 9000 is the time of peak velocity.

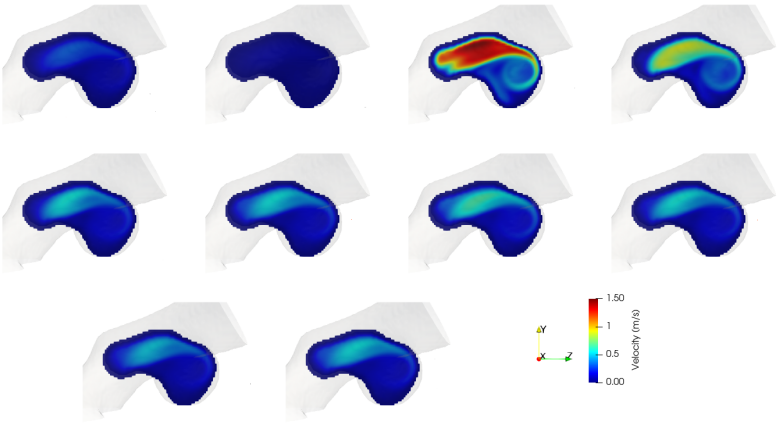

Figure 3.11. C0067 Flow Velocity z-plane slice at timesteps (from left to right) 8200, 8600, 9000, 9400, 9800, 10200, 10600, 11000, 11400, and 11800; where 9000 is the time of peak velocity.

Patient C0067's aneurysm is one of the smallest cases, and as can be seen from the simulation snapshots in Figure 3.11, blood completely fills the aneurysm. The same whirlpool-like motion mentioned in some of the previous cases is present. The flow velocity inside C0067's aneurysm is maintained much longer than the other aneurysms. The small size of this aneurysm most likely contributes to this conservation. It is also worth noting that C0067's aneurysm is the smallest by volume of the cases mentioned in this report.

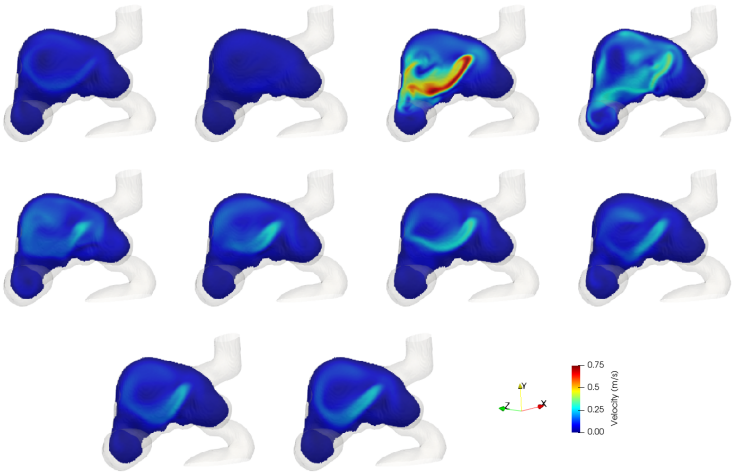

Figure 3.12. C0075 Flow Velocity xz-plane slice at timesteps (from left to right) 8399, 8799, 9199, 9599, 9999, 10399, 10799, 11199, 11599, and 11999; where 9199 is the time of peak velocity.

In patient C0075's aneurysm, blood fills the majority of the aneurysm as the vessel clips the bottom of this bifurcation aneurysm. Flow is seemingly unstable at certain time steps. Flow velocity inside an aneurysm is a lot less than many of the other aneurysms. This is most likely due to the size of the aneurysm. It is also worth mentioning that this aneurysm is essentially tied for the largest aneurysm by volume with C0036's aneurysm.

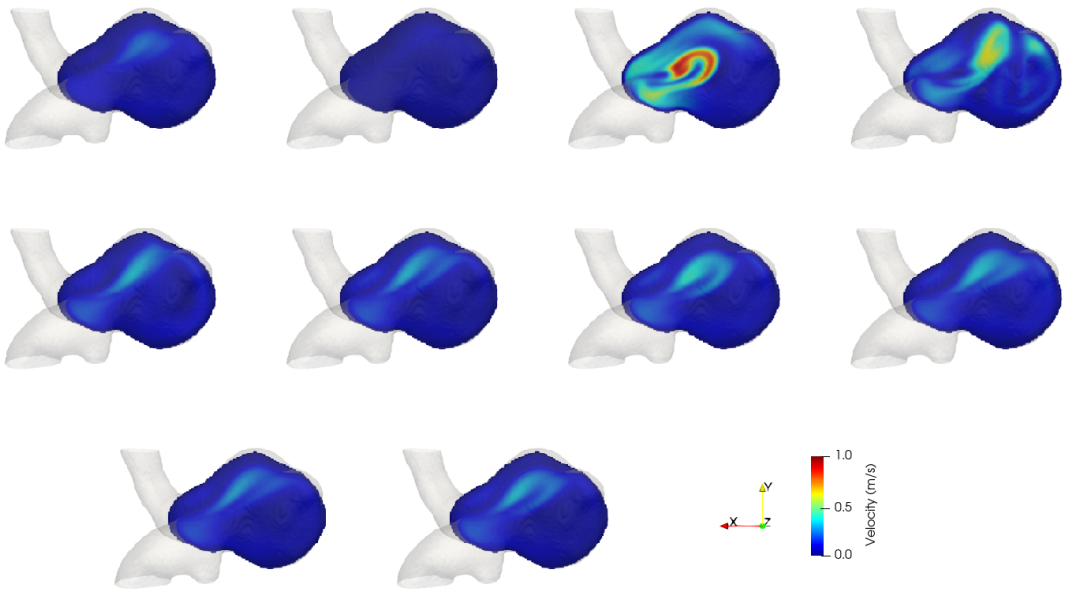

Figure 3.13. C0085 Flow Velocity z-plane slice at timesteps (from left to right) 8200, 8600, 9000, 9400, 9800, 10200, 10600, 11000, 11400, and 11800; where 9000 is the time of peak velocity.

Blood flow in patient C0085's aneurysm, Figure 3.13, unlike the majority of the other cases in this report doesn't have that typical whirlpool-like motion. Instead, C0085's aneurysm blood flow has a corkscrew-like motion, with the spiral motion increasing in its diameter as it moves away from the inflow jet before its eventual decay. This phenomenon is supported by the DMD modes in Figure 3.35. It is also worth mentioning that it appears that this patient might be developing a second aneurysm that may or not merge with this one.

In the sidewall aneurysm from patient C0088, case C0088b, the blood partially fills the aneurysm moving in a spiral motion. Unlike the other patients, C0088 had two aneurysms one which was a sidewall aneurysm and the other a terminal aneurysm. With patient C0088 having two

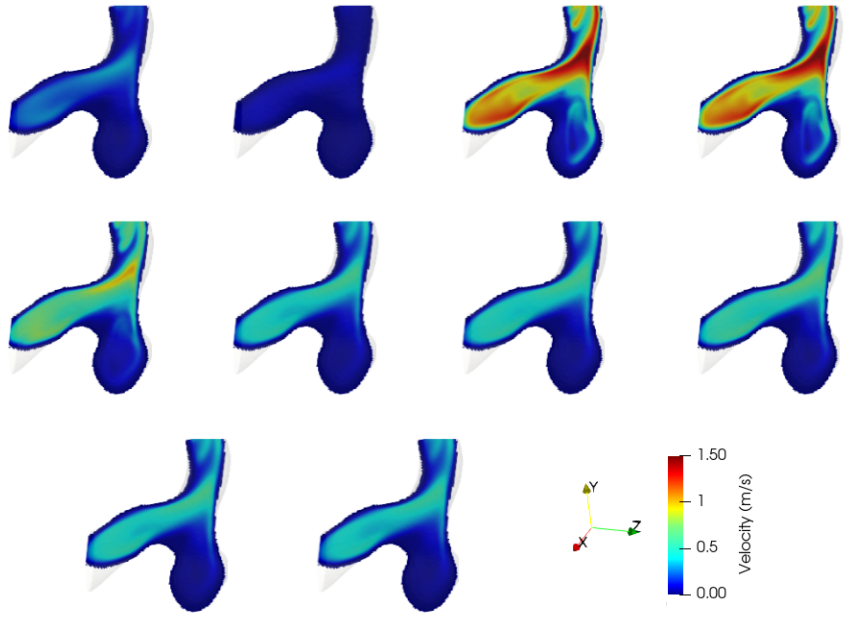

Figure 3.14. C0088b Flow Velocity xyz-plane slice at timesteps (from left to right) 8200, 8600, 9000, 9400, 9800, 10200, 10600, 11000, 11400, and 11800; where 9000 is the time of peak velocity.

aneurysms, it is unclear what effect the other aneurysm has on the inlet conditions of C0088b since both are in close proximity.

3.2.2. Three-dimensional flow structures

Each of the following three-dimensional flow structures was generated in Paraview following several steps. First, for each case, its Result files were imported into Paraview. Secondly, the contour of each aneurysm was visualized using the built-in cell data point data converter and contour filters. Then, each aneurysm was isolated from the parent artery; this process was shown in Figure 2.3 and explained in step 3 of section 2.5. Unlike with setting up for the DMD analysis, the unconnected parts of the parent artery can be safely removed as the visualization can be done solely in Paraview. Finally, the built-in streamline filter is applied to the flow field data.

Figure 3.15, shows the velocity streamlines of the flow pattern inside patient C0002's aneurysm. Here the circular motion mentioned with the other aneurysm cases is presented contradictory what is shown by slice views seen in Figure 3.4. This isn't all that surprising as the slice views cannot capture as much of the flow patterns in the aneurysm as the three-dimensional streamline views can. Additionally, in this illustration, we can the flow velocities in the parent artery are more or

less conserved. Thus, the blood flow here is essentially stable as flow velocities in the parent artery are conserved.

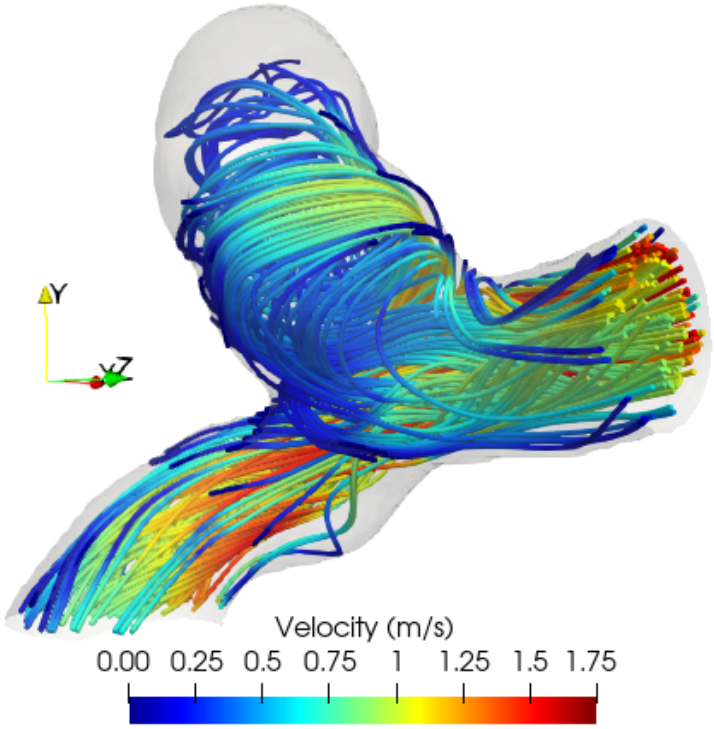

Figure 3.15. Flow pattern inside C0002's aneurysm. The velocity field at the peak systole is visualized by the streamlines.

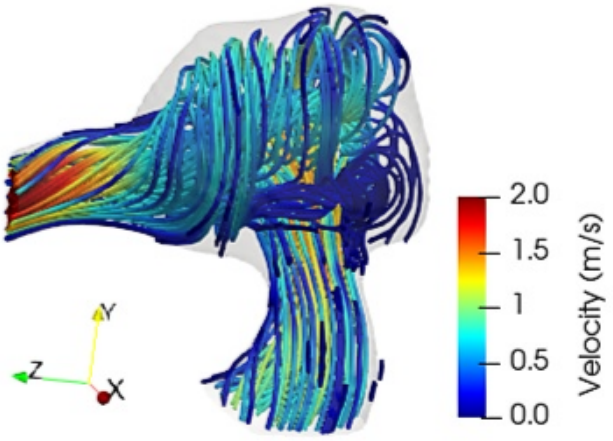

Figure 3.16. Flow pattern inside C0006's aneurysm. The velocity field at the peak systole is visualized by the streamlines.

However, when taking a look at the three-dimensional velocity streamlines of the blood flow inside patient C0006's aneurysm in Figure 3.16, this further supports the flow patterns depicted in this aneurysm's slice views seen in Figure 3.5. Additionally, the flow seems to destabilize a little; this destabilization was not clear in the slice views. In the next section, it becomes more clear that the flow in this aneurysm destabilizes as shown by this case's DMD modes in Figure 3.27.

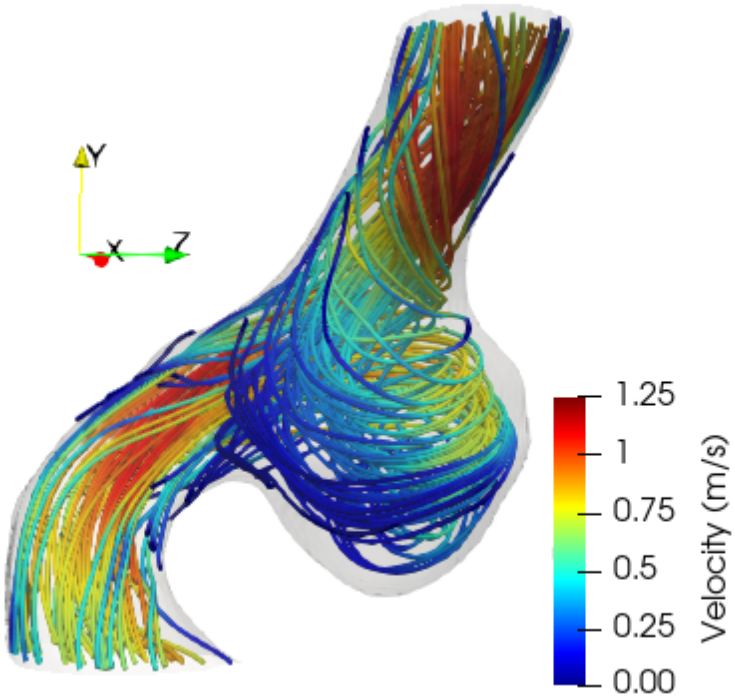

Figure 3.17. Flow pattern inside C0014's aneurysm. The velocity field at the peak systole is visualized by the streamlines.

The three-dimensional velocity streamlines of the blood flow inside patient C0014's aneurysm seen in 3.17, agrees with what was shown in Figure 3.6. Also, the exact point at which the inflow jet enters the aneurysm is more clear and confirms that it does enter the aneurysm in close proximity to the outflow jet. Similarly to the flow inside C0002's aneurysm, the flow velocities in the parent artery of C0014's aneurysm appear to be conserved. Again, the blood flow here is essentially stable as flow velocities in the parent artery are conserved.

The erratic flow pattern of the blood in patient C0016's aneurysm mentioned in the previous section is confirmed by the three-dimensional velocity streamlines of the blood flow illustrated in Figure 3.18. Despite this erratic flow, the blood flow here is essentially stable as flow velocities in the parent artery are conserved. Additionally, the overall blood velocities, in this case, are lowest in comparison to the other cases.

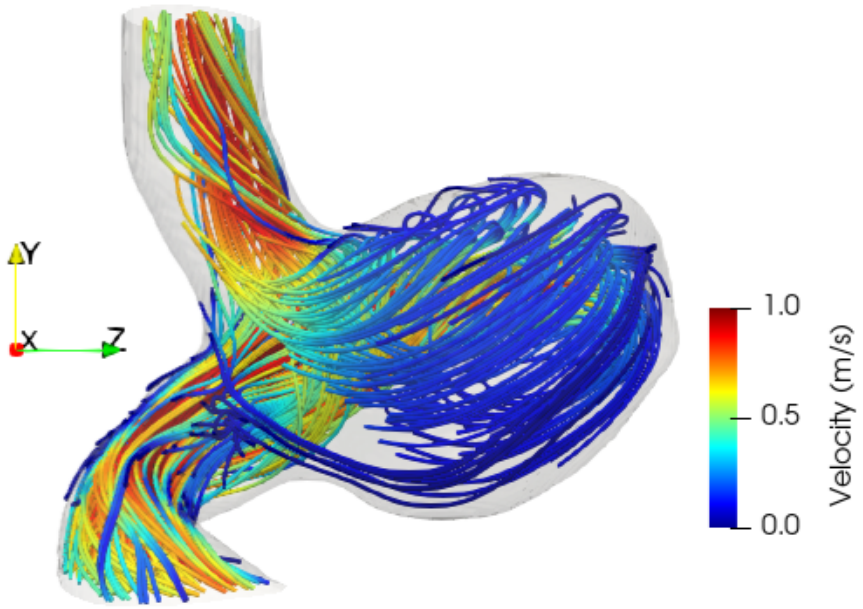

Figure 3.18. Flow pattern inside C0016's aneurysm. The velocity field at the peak systole is visualized by the streamlines.

The whirlpool motion mentioned for the blood flow pattern in C0034's aneurysm, mentioned in the previous section, is better shown by the three-dimensional velocity streamlines portrayed in Figure 3.19. Flow moving to the aneurysm is slower than flow leaving the aneurysm confirming the momentum build-up that was previously mentioned. This increase in flow velocity in turn causes the flow to become unstable.

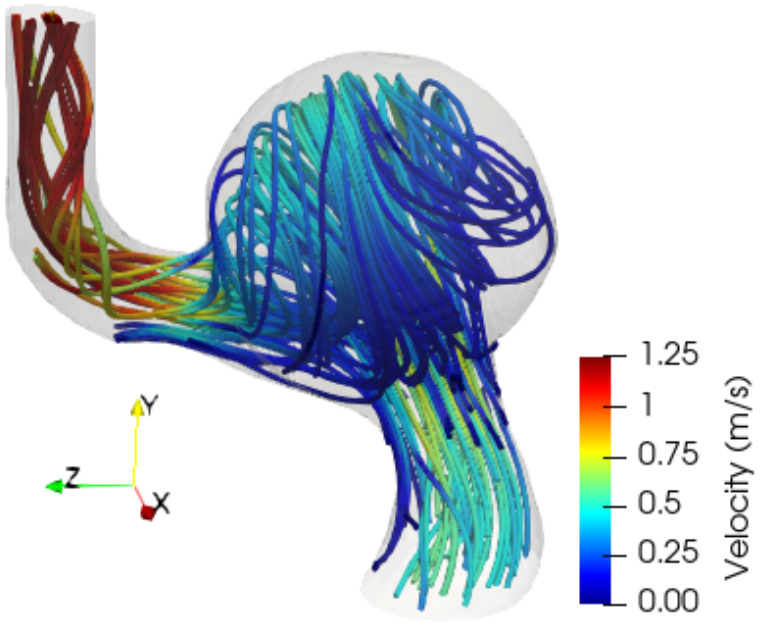

Figure 3.19. Flow pattern inside C0034's aneurysm. The velocity field at the peak systole is visualized by the streamlines.

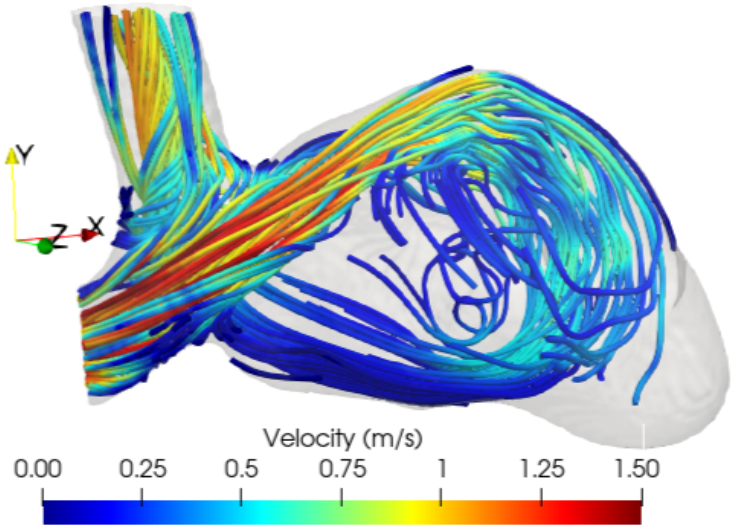

Figure 3.20. Flow pattern inside C0036's aneurysm. The velocity field at the peak systole is visualized by the streamlines.

Blood flow inside patient C0036's aneurysm appears to be unstable as depicted by the three-dimensional velocity streamlines in Figure 3.20. This destabilization of the flow is supported by the analysis of the DMD modes for this case in the next section. Furthermore, the aneurysm also appears to be only partially filled. However, the corkscrew-like motion isn't as clear in this view as it was in the slice views as shown in Figure 3.9.

From the three-dimensional streamlines of the blow flow in patient C0042's aneurysm shown in Figure 3.21, the whirlpool motion can be seen which wasn't the case in the corresponding slice views shown in Figure 3.10. On the other hand, flow velocities in the parent are not conserved as the flow entering the aneurysm is greater than the flow leaving the aneurysm.

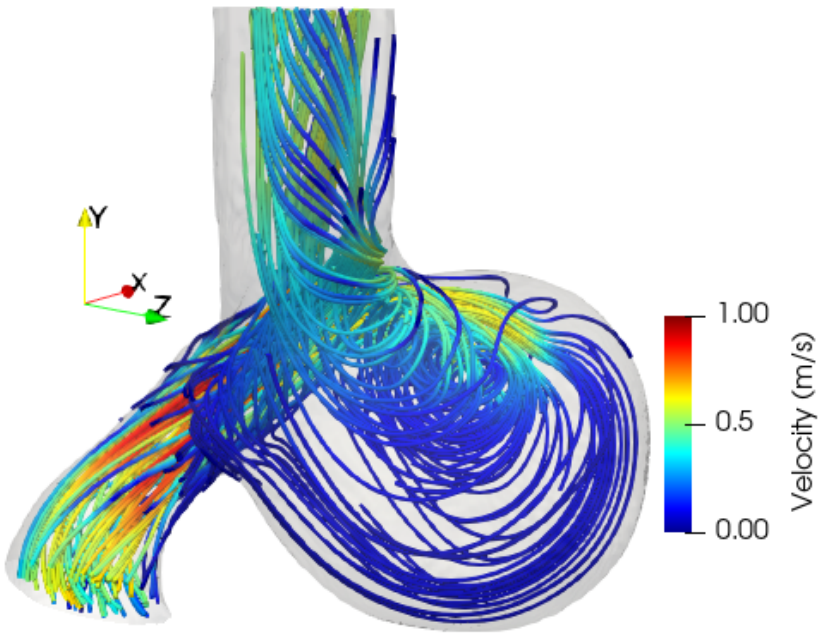

Figure 3.21. Flow pattern inside C0042's aneurysm. The velocity field at the peak systole is visualized by the streamlines.

Unlike the slice views for patient C0067's aneurysm shown in Figure 3.11, the flow portrayed by the three-dimensional velocity streamlines shown in Figure 3.22 seems to destabilize. This contradiction is most likely due to how small this aneurysm is. Also, it is unclear if the flow velocities in the parent artery are conserved.

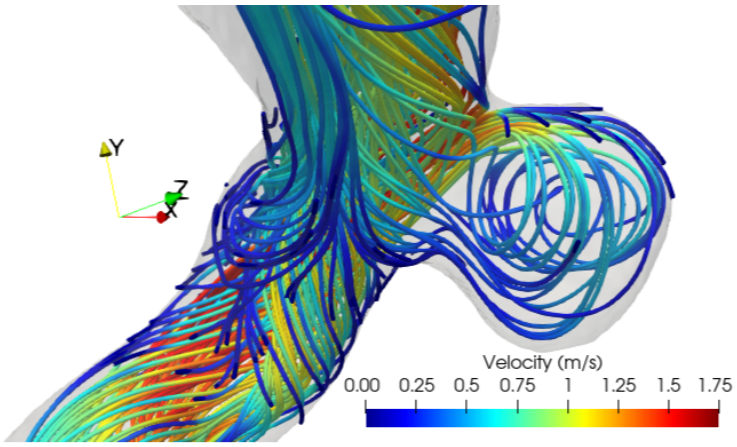

Figure 3.22. Flow pattern inside C0067's aneurysm. The velocity field at the peak systole is visualized by the streamlines.

Blood flow in patient C0075's aneurysm, according to the three-dimensional velocity streamlines shown in Figure 3.23, is highly unstable confirming what was discussed previously for this case. The three-dimensional velocity streamlines just so happen to capture this instability better than the slice views in Figure 3.12 were able to. Which isn't all too surprising. Additionally, flow velocities in the parent artery are not conserved.

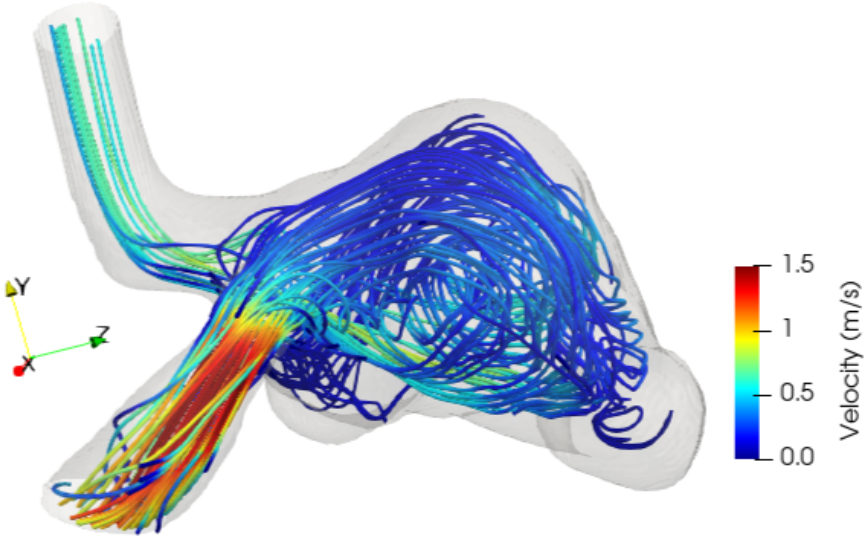

Figure 3.23. Flow pattern inside C0075's aneurysm. The velocity field at the peak systole is visualized by the streamlines.

According to the three-dimensional velocity streamlines of the blood flow, flow in C0085's aneurysm is highly unstable as depicted in Figure 3.24. This instability was not clear in corresponding the slice views in Figure 3.13. Additionally, the tiny bulge on the parent artery is shown to play a role in the flow patterns, thus this patient does have a second aneurysm despite the source data stating otherwise. Further investigation of C0085's secondary aneurysm should be considered in future works.

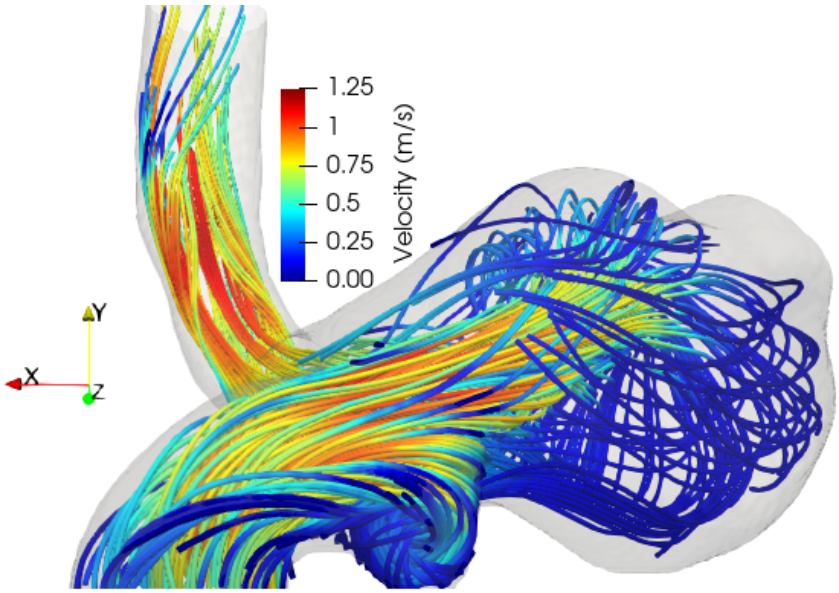

Figure 3.24. Flow pattern inside C0085's aneurysm. The velocity field at the peak systole is visualized by the streamlines.

Unlike patient C0085, patient C0088 clearly has two aneurysms, hence the 'b' designation C0088b. However, only C0088b is discussed as the other is not a sidewall aneurysm. As shown by the three-dimensional velocity streamlines for C0088b in Figure 3.25, blood flow does not completely fill the aneurysm coinciding with what was mentioned in the previous section regarding the slice views depicted in Figure 3.14. Again, since patient C0088 has two aneurysms, it is unclear what effect the other aneurysm has on C0088b.

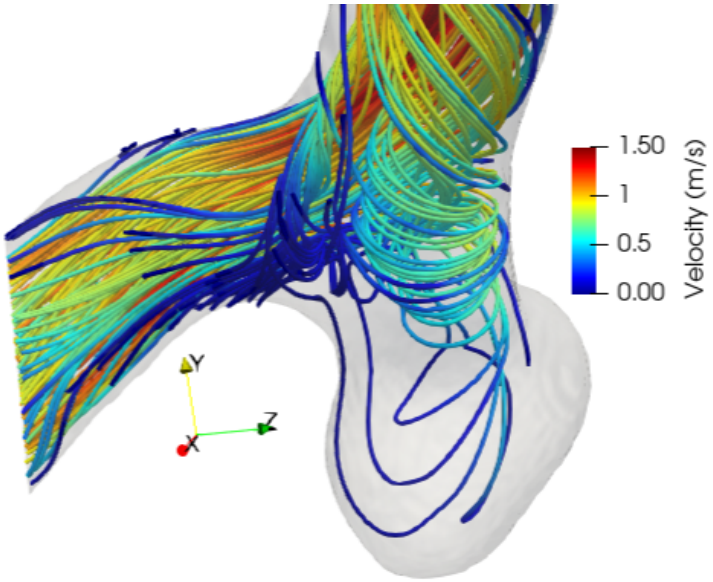

Figure 3.25. Flow pattern inside C0088's sidewall aneurysm, C0088b. The velocity field at the peak systole is visualized by the streamlines.

3.3. DMD analysis

For each patient, the aneurysm mesh was kept with no down-scaling and the data cells were written to .csv files. Due to the large size of several .csv files, some upwards of approximately 10 GB, the DMD Matlab code was run on the NDSU CCAST server.

From the CFD simulation results, the DMD analysis is carried out for both patients. In these cases, the total number of snapshots is maximum at $n = 40$. The distribution of the discrete-time eigenvalues λ_k in the complex plane shows that there exist eigenvalues in the interior part of the unit circle. The modes associated with these eigenvalues are damped quickly with time. Their magnitudes can be large but they contribute to the flow dynamics in a short period of time. Therefore, this justifies the use of the scaled magnitude $|\lambda_k^n b_k|$ to identify the dominant modes.

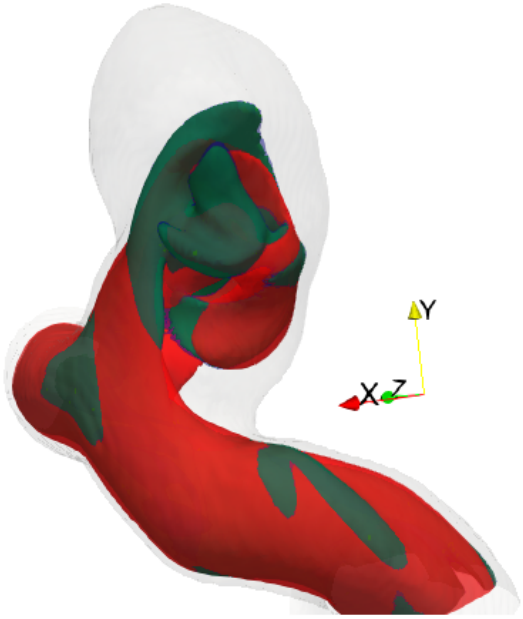

Figure 3.26. C0002 DMD modes 1 (red), 2 (green), and 3 (blue). Modes 2 and 3 almost completely overlap for this case, hence why only specs of blue can be seen.

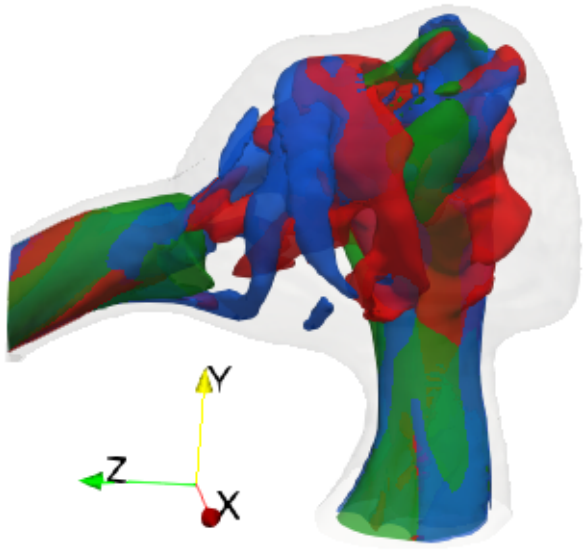

Figure 3.27. C0006 DMD modes 1 (red), 2 (green), and 3 (blue).

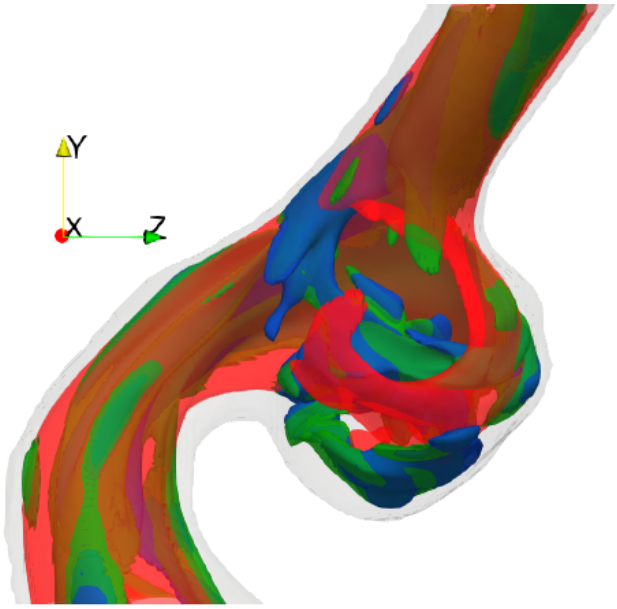

Figure 3.28. C0014 DMD modes 1 (red), 2 (green), and 3 (blue).

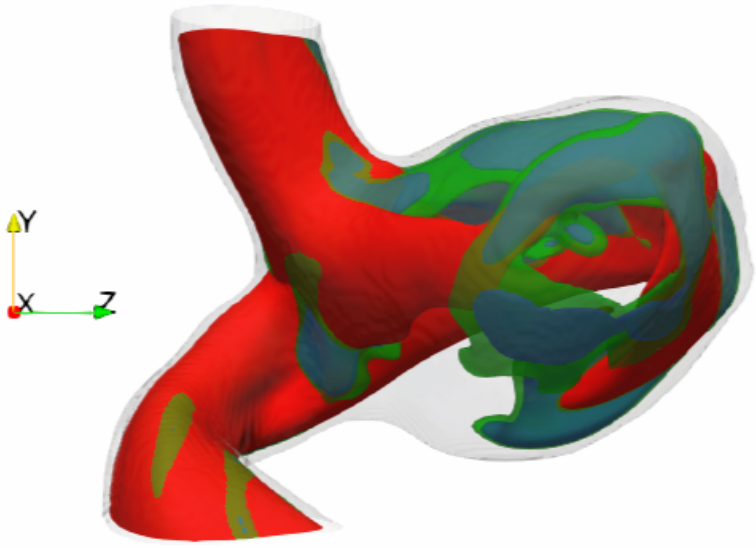

Figure 3.29. C0016 DMD modes 1 (red), 2 (green), and 3 (blue).

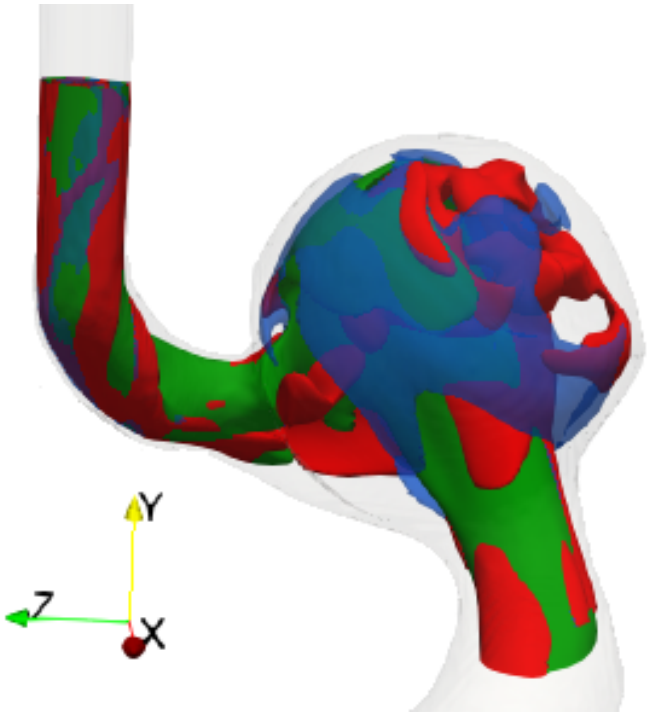

Figure 3.30. C0034 DMD modes 1 (red), 2 (green), and 3 (blue).

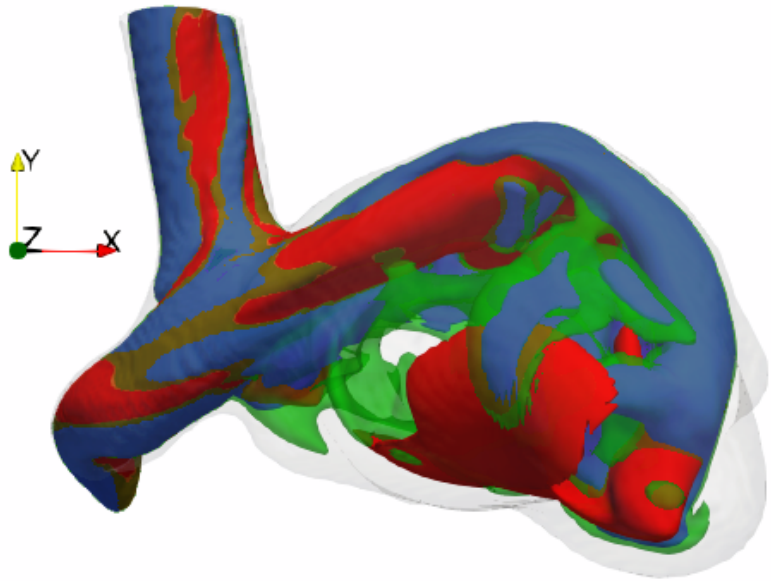

Figure 3.31. C0036 DMD modes 1 (red), 2 (green), and 3 (blue).

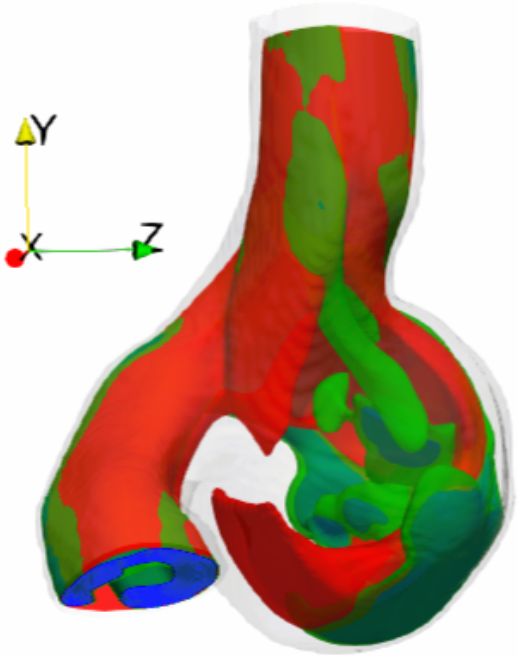

Figure 3.32. C0042 DMD modes 1 (red), 2 (green), and 3 (blue).

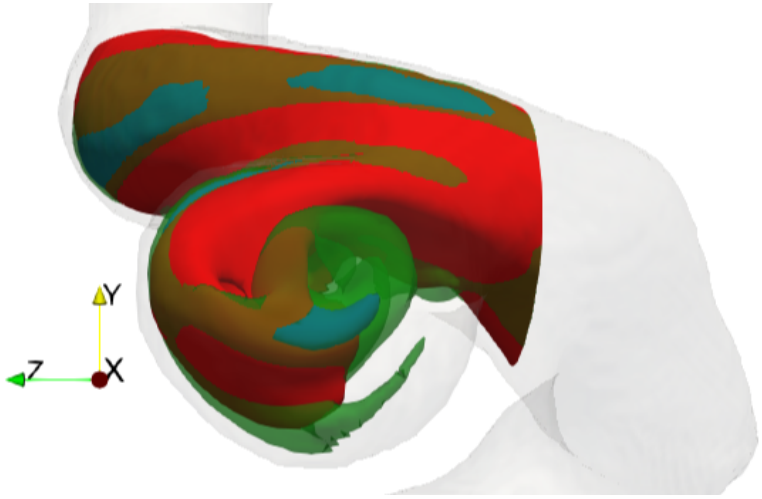

Figure 3.33. C0067 DMD modes 1 (red), 2 (green), and 3 (blue).

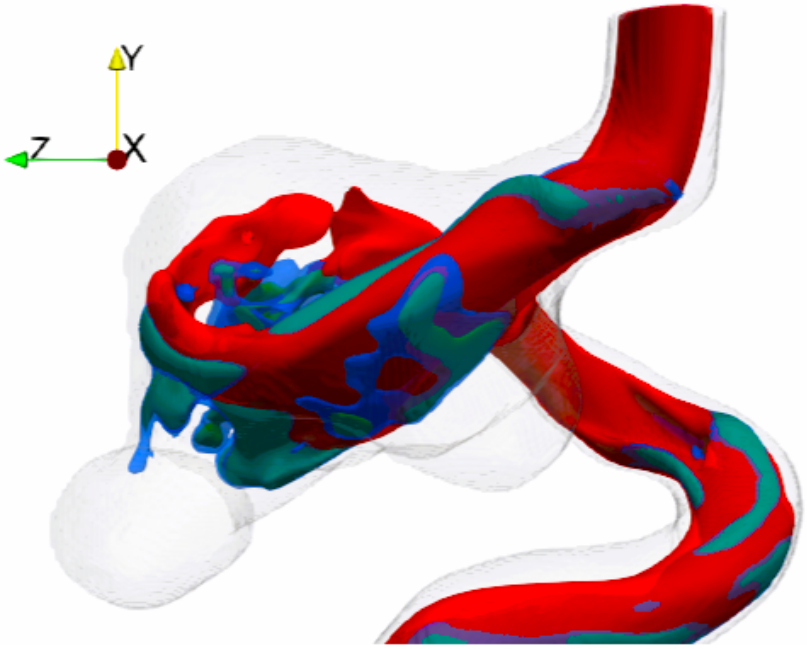

Figure 3.34. C0075 DMD modes 1 (red), 2 (green), and 3 (blue).

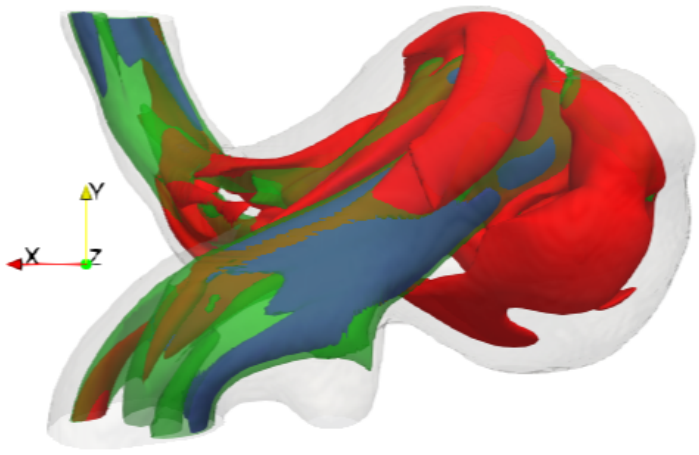

Figure 3.35. C0085 DMD modes 1 (red), 2 (green), and 3 (blue).

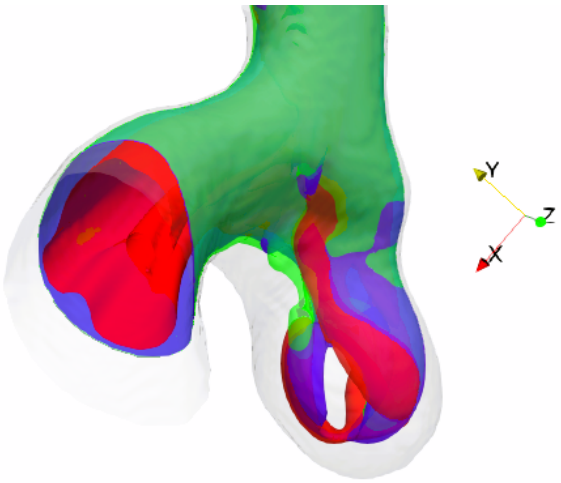

Figure 3.36. C0088b DMD modes 1 (red), 2 (green), and 3 (blue).

The Computational Fluid Dynamics and the DMD simulations show the hemodynamic conditions inside the aneurysms are dominated by the inflow jet. In C0002's aneurysm (Figure 3.26), is very hard to tell what is going on with the inflow jet, however, it seems to collide against the distal wall but fails to fill the entire aneurysm. The inflow jet in C0006 (Figure 3.27), is shown to collide against the aneurysm wall head-on causing the flow to destabilize as it spirals out of the aneurysm. In case C0014 (Figure 3.28), the flow is more stable as the primary mode for each can capture the majority of the overall fluid flow. Consequently, the inflow jet in case C0014 enters the aneurysm off to one side. Similarly, in case C0016 (Figure 3.29), the flow is again more stable as the primary mode for each can capture the overall fluid flow. However, the flow isn't nearly as stable as the flow in case C0014.

Case 0034 (Figure 3.30), on the other hand, shares more similarities with case C0014 in that it appears to be very stable. The inflow jet for C0034 enters the aneurysm from the dorsal side. Since both cases C0014's and case C0034's inflow jets collide with the distal at an offset point instead of a more central point, they don't destabilize like case C0006's flow does. The reason flow in case C0016 is less stable than C0014 and C0034 is probably because of how close the inflow jet is in proximity to the outflow jet.

Flow in case C0036 (Figure 3.31) appears to destabilize as it spirals back towards the outflow jet. Even though the inflow jet of this case is in close proximity to the outflow jet, nearly the entire

aneurysm is filled. For case C0042 (Figure 3.32), the inflow jet hit the aneurysm wall so close to the proximity of the outflow jet that it appears as if back-flow from the outflow jet is what fills this aneurysm. Similarly to case C0016 and case C0036, the proximity of the inflow jet in relation to the outflow jet in case C0042 contributes why the flow destabilizes.

Case C0067's (Figure 3.33) inflow jet appears to be the most stable. This is probably to the fact of how small the aneurysm, in this case, is which in turn compresses the flow inside the aneurysm in a tight bundle. Even though the inflow jet and the outflow jet of this case are in close proximity, the small diameter of this aneurysm seems to prevent the flow from destabilizing as much as would be expected. Case C0002, previously mentioned has a similar diameter to this case despite it being larger. Thus, it seems the diameter of the aneurysm may play a bigger role than the height of the aneurysm in determining flow stability.

Case C0075 (Figure 3.34) differs from all the other cases in that this aneurysm is a bifurcation aneurysm. This in turn destabilizes the flow in C0075, however, the destabilization is not as much as one would expect considering blood mainly fills the aneurysm where the aneurysm starts to branch off. The two branches themselves appear untouched for the most part. In case C0085 (Figure 3.35), the corkscrew-like motion shown in Figure 3.13 can also be seen in the DMD modes. The flow, in this case, appears to be stable with the primary mode capturing the majority of the fluid flow. Case C0088b (Figure 3.36) inflow jet hits the distal wall of the aneurysm near where the outflow jet is located as a result the aneurysm is only partially filled. Unlike any of the other aneurysms mentioned in this report, C0088b is one of two aneurysms for this patient, therefore, it is unclear what effect the other aneurysm has on this one making any conclusions made here inaccurate.

For each case, three dominant modes show that the inflow jet first impinges on the distal wall and then follows the wall curvature to return to the proximal neck. Thus, the spatial coverage of DMD modes is useful in characterizing the overall three-dimensional structures of the inflow jet. Additionally, the location of where the inflow jet hits the distal wall affects the behavior of the outflow.

3.3.1. DMD Spectra

For each aneurysm case, the frequency of their modes was computed. This computation was done using the following code in the Matlab console.

```
% modal freq computation
load("Analysis_Results.mat");
load("Spectrum.mat");
spectra = Spectrum{1,1}.sigma;
% Spectrum{1,1} is where the spectrum data for L=1 is stored. L=2 can be ignored
% sigma is the frequencies
spectra=sort(spectra);
% displays the frequencies of the first three modes
spectra(1:3)
% 1:3 refer to modes 1-3.
```

The results of this code are listed in the table below.

Table 3.1. Modal frequencies generated from Matlab code. Primary mode, secondary mode, and tertiary mode correspond to modes 1, 2, and 3 respectively.

Patient ID	Primary Mode	Secondary Mode	Tertiary Mode	Ruptured
C0002	0.7599 Hz	0.8524 Hz	0.8769 Hz	No
C0006	2.1416 Hz	3.2146 Hz	4.6010 Hz	No
C0014	2.4828 Hz	5.0205 Hz	6.1727 Hz	No
C0034	1.6250 Hz	2.8206 Hz	3.1142 Hz	No
C0036	3.9510 Hz	5.8047 Hz	6.1111 Hz	No
C0042	0.8319 Hz	0.8884 Hz	1.0660 Hz	No
C0067	0.2171 Hz	0.4398 Hz	0.5370 Hz	No
C0075	6.8569 Hz	13.6171 Hz	17.3059 Hz	No
C0085	2.6517 Hz	3.5862 Hz	3.6765 Hz	Yes
C0088b	0.0437 Hz	0.0483 Hz	0.1076 Hz	No

4. CONCLUSIONS

Intracranial aneurysm is a common cerebrovascular disorder that causes swelling in the blood vessels of the brain [32]. This disorder is thought to be present in approximately 2% to 5% of adults worldwide [32]. Nearly all aneurysms are discovered purely by accident. Brain aneurysms cause problems such as pressing up against cranial nerves or hemorrhaging [13, 23, 24]. Aneurysms can also leak blood into the brain or rupture which can cause hemorrhaging [13, 23]. If an aneurysm ruptures, it can pose life-threatening consequences. Therefore, rupture risk analysis of existing aneurysm(s) in a patient is crucial.

Current risk factor calculators take into account the patient's history, the configuration of the aneurysm in space, and its complexity [12, 13]. Due to the complexity of some aneurysms, finding the right treatment can be a challenge. Ultimately, treatment decisions are often based on a neurosurgeon's preference and intuition as the treatment process is often challenging due to the microsurgeries that are required [24]. This approach is not very patient-specific.

Medical imaging already is being used to compute blood flow in brain aneurysms using medical images such as Computed Tomography (CT) or Magnetic Resonance Imaging (MRI) [5, 24, 35, 36], which allows the computation of velocity and pressure fields to be expressed in great detail. Additionally, it has been shown that wall shear stress is associated with the growth and rupture of an intracranial aneurysm which in turn can be indirectly captured by hemodynamics using image-based CFD [29, 38]. And yet, risk factor calculators lack necessary data related to intra-aneurysmal blood flow dynamics [24]. Despite this, there is a large gap between numerical simulation and clinical practice [4, 39] because it is challenging to analyze blood flow dynamics in complex geometries of brain aneurysms.

Even though there is a great need for analyzing inflow jet dynamics in clinical practice, data summarized in DICOM files are usually limited to the geometrical view of the aneurysm. This approach is essentially what is called a black-box approach in that you can only measure the anatomy and not the blood flow dynamics; thus, it cannot account for internal hemodynamics.

In our work, computational fluid dynamics simulations were run to produce reliable and invaluable data for analysis of the fluid flow in patient-specific models of aneurysms. Then, DMD

was used to identify the dominant features of the blood flow in brain aneurysms. Our results show that DMD is an essential tool for analyzing blood flow patterns of brain aneurysms because DMD can provide great details of the flow including the dominant frequencies. It is evident that aneurysm geometry has a dominating effect on the resulting frequencies of the jet. Our results suggest that these dominating frequencies might be used to identify the transition of the incoming jet to turbulence in the neck region. Therefore, the use of DMD for analyzing blood flow patterns should be considered in future works.

REFERENCES

[1] N. Bessonov, A. Sequeira, S. Simakov, Yu. Vassilevskii, and V. Volpert. Methods of blood flow modelling. *Mathematical Modelling of Natural Phenomena*, 11(1):1–25, 2015.

[2] J. P. Bonnet, J. Delville, M. N. Glauser, R. A. Antonia, D. K. Bisset, D. R. Cole, H. E. Fiedler, J. H. Garem, D. Hilberg, J. Jeong, and et al. Collaborative testing of eddy structure identification methods in free turbulent shear flows. *Experiments in Fluids*, 25(3):197–225, 1998.

[3] Garry L. Brown and Anatol Roshko. On density effects and large structure in turbulent mixing layers. *Journal of Fluid Mechanics*, 64(4):775–816, 1974.

[4] J.R. Cebral and H. Meng. Counterpoint: Realizing the clinical utility of computational fluid dynamics—closing the gap. *American Journal of Neuroradiology*, 33(3):396–398, 2012.

[5] Juan R. Cebral, Marcelo A. Castro, James E. Burgess, Richard S. Pergolizzi, Michael J. Sheridan, and Christopher M. Putman. Characterization of cerebral aneurysms for assessing risk of rupture by using patient-specific computational hemodynamics models, Nov 2005.

[6] Juan R Cebral, Marcelo A Castro, James E Burgess, Richard S Pergolizzi, Michael J Sheridan, and Christopher M Putman. Characterization of cerebral aneurysms for assessing risk of rupture by using patient-specific computational hemodynamics models. *American Journal of Neuroradiology*, 26(10):2550–2559, 2005.

[7] Kevin K. Chen, Jonathan H. Tu, and Clarence W. Rowley. Variants of dynamic mode decomposition: Boundary condition, koopman, and fourier analyses. *Journal of Nonlinear Science*, 22(6):887–915, 2012.

[8] Ronak Dholakia, Chander Sadasivan, David J. Fiorella, Henry H. Woo, and Baruch B. Lieber. Hemodynamics of flow diverters. *Journal of Biomechanical Engineering*, 139(2), 2017.

[9] Carl Eckart and Gale Young. The approximation of one matrix by another of lower rank. *Psychometrika*, 1(3):211–218, 1936.

[10] Juhana Frösen, Riikka Tulamo, Anders Paetau, Elisa Laaksamo, Miikka Korja, Aki Laakso, Mika Niemelä, and Juha Hernesniemi. Saccular intracranial aneurysm: pathology and mechanisms. *Acta Neuropathologica*, 123(6):773–786, 2012.

[11] Anvar Gilmanov, Trung Bao Le, and Fotis Sotiropoulos. A numerical approach for simulating fluid structure interaction of flexible thin shells undergoing arbitrarily large deformations in complex domains. *Journal of computational physics*, 300:814–843, 2015.

[12] Christopher A. Hilditch, Waleed Brinjikji, Anderson Tsang, Patrick Nicholson, Alex Kostynskyy, Michael Tymianski, Timo Krings, Ivan Radovanovic, and Vitor Pereira. Application of phases and elapss scores to ruptured cerebral aneurysms: How many would have been conservatively managed? *Journal of Neurosurgical Sciences*, 65(1), 2021.

[13] M.O. Khan, V. Toro Arana, M. Najafi, D.E. MacDonald, T. Natarajan, K. Valen-Sendstad, and D.A. Steinman. On the prevalence of flow instabilities from high-fidelity computational fluid dynamics of intracranial bifurcation aneurysms. *Journal of Biomechanics*, 127:110683, Aug 2021.

[14] Trung B Le, Iman Borazjani, and Fotis Sotiropoulos. Pulsatile flow effects on the hemodynamics of intracranial aneurysms. *Journal of biomechanical engineering*, 132(11):111009, 2010.

[15] Trung B Le, Daniel R Troolin, Devesh Amatya, Ellen K Longmire, and Fotis Sotiropoulos. Vortex phenomena in sidewall aneurysm hemodynamics: experiment and numerical simulation. *Annals of biomedical engineering*, 41(10):2157–2170, 2013.

[16] Trung Bao Le, Iman Borazjani, Seokkoo Kang, and Fotis Sotiropoulos. On the structure of vortex rings from inclined nozzles. *Journal of fluid mechanics*, 686:451, 2011.

[17] Trung Bao Le, Ariel Christenson, Toni Calderer, Henryk Stolarski, and Fotis Sotiropoulos. A thin-walled composite beam model for light-weighted structures interacting with fluids. *Journal of Fluids and Structures*, 95:102968, 2020.

[18] Trung Bao Le, Mohammed SM Elbaz, Rob J Van Der Geest, and Fotis Sotiropoulos. High resolution simulation of diastolic left ventricular hemodynamics guided by four-dimensional flow magnetic resonance imaging data. *Flow, Turbulence and Combustion*, 102(1):3–26, 2019.

[19] Trung Bao Le and Fotis Sotiropoulos. Fluid–structure interaction of an aortic heart valve prosthesis driven by an animated anatomic left ventricle. *Journal of computational physics*, 244:41–62, 2013.

[20] Fuyou Liang, Kazuaki Fukasaku, Hao Liu, and Shu Takagi. A computational model study of the influence of the anatomy of the circle of willis on cerebral hyperperfusion following carotid artery surgery. *BioMedical Engineering OnLine*, 10(1):84, 2011.

[21] Daniel E. MacDonald, Mehdi Najafi, Lucas Temor, and David A. Steinman. Spectral bandedness in high-fidelity computational fluid dynamics predicts rupture status in intracranial aneurysms. *Journal of Biomechanical Engineering*, 144(6), Jan 2022.

[22] Mayo Clinic. Brain aneurysm - diagnosis and treatment, April 2022. `https://www.mayoclinic.org/diseases-conditions/brain-aneurysm/diagnosis-treatment/drc-20361595`.

[23] Mayo Clinic. Brain aneurysm - symptoms and causes, April 2022. `https://www.mayoclinic.org/diseases-conditions/brain-aneurysm/symptoms-causes/syc-20361483`.

[24] Vitaliy L. Rayz and Aaron A. Cohen-Gadol. Hemodynamics of cerebral aneurysms: Connecting medical imaging and biomechanical analysis. *Annual Review of Biomedical Engineering*, 22(1):231–256, 2020.

[25] Gabriel J. Rinkel, Mamuka Djibuti, Ale Algra, and J. van Gijn. Prevalence and risk of rupture of intracranial aneurysms. *Stroke*, 29(1):251–256, 1998.

[26] Clarence W. Rowley, Igor Mezić, Shervin Bagheri, Philipp Schlatter, and Dan S. Henningson. Spectral analysis of nonlinear flows. *Journal of Fluid Mechanics*, 641(1):115–127, 2009.

[27] M. Samimy, K. S. Breuer, L. G. Leal, and P. H. Steen. *A Gallery of Fluid Motion*. Cambridge University Press, 2003.

[28] Wouter I. Schievink. Intracranial aneurysms. *New England Journal of Medicine*, 336(1):28–40, 1997.

[29] Daniel M Sforza, Christopher M Putman, and Juan Raul Cebral. Hemodynamics of cerebral aneurysms. *Annual review of fluid mechanics*, 41:91–107, 2009.

[30] Kunihiko Taira, Steven L Brunton, Scott TM Dawson, Clarence W Rowley, Tim Colonius, Beverley J McKeon, Oliver T Schmidt, Stanislav Gordeyev, Vassilios Theofilis, and Lawrence S Ukeiley. Modal analysis of fluid flows: An overview. *Aiaa Journal*, pages 4013–4041, 2017.

[31] F. P. Tan, N. B. Wood, G. Tabor, and X. Y. Xu. Comparison of les of steady transitional flow in an idealized stenosed axisymmetric artery model with a rans transitional model. *Journal of Biomechanical Engineering*, 133(5), 2011.

[32] B G Thompson, R D Brown, S Amin-Hanjani, J P Broderick, and K M Cockroft. Guidelines for the management of patients with unruptured intracranial aneurysms: a guideline for healthcare professionals from the american heart association/american stroke association. *Stroke*, 46, 2015.

[33] Gabor Toth and Russell Cerejo. Intracranial aneurysms: Review of current science and management. *Vascular Medicine*, 23(3):276–288, 2018.

[34] L. N. Trefethen and D. Bau. *Numerical Linear Algebra*. SIAM, 2009.

[35] Monique HM Vlak, Ale Algra, Raya Brandenburg, and Gabriël JE Rinkel. Prevalence of unruptured intracranial aneurysms, with emphasis on sex, age, comorbidity, country, and time period: a systematic review and meta-analysis. *The Lancet Neurology*, 10(7):626–636, 2011.

[36] Bryce Weir. Unruptured intracranial aneurysms: a review. *Journal of Neurosurgery*, 96(1):3–42, 2002.

[37] John F. Wendt and John David Anderson. *Computational Fluid Dynamics: An introduction*. Springer, 2009.

[38] Xiaolin Wu, Stefanie Gürzing, Christiaan Schinkel, Merel Toussaint, Romana Perinajová, Pim van Ooij, and Saša Kenjereš. Hemodynamic study of a patient-specific intracranial aneurysm: Comparative assessment of tomographic piv, stereoscopic piv, in vivo mri and computational fluid dynamics. *Cardiovascular Engineering and Technology*, 2021.

[39] J. Xiang, V.M. Tutino, K.V. Snyder, and H. Meng. Cfd: Computational fluid dynamics or confounding factor dissemination? the role of hemodynamics in intracranial aneurysm rupture risk assessment. *American Journal of Neuroradiology*, 35(10):1849–1857, 2013.